WAVES IN RANDOM AND COMPLEX MEDIA

https://www.tandfonline.com/journals/twrm20

Impact factor = 4.853

Accepted July 12th 2022

Magnetized Supercritical Third-Grade Nanofluid Flow from a Vertical Cylinder Using a Crank-Nicolson Implicit Scheme

Ashwini Hiremath1, G. Janardhana Reddy2 *, Hussain Basha3, N. S. V. Narayanan4 and O. Anwar Bég5

1) Ashwini Hiremath
Position: *Research Student*
Address: *Department of Mathematics, Central University of Karnataka, Kalaburagi, India.*
Email: *ashwini.mathad67@gmail.com*

2) Dr. G. Janardhana Reddy (Corresponding Author)
Position: *Assistant Professor,*
Address: *Department of Mathematics, Central University of Karnataka, Kalaburagi, India.*
Email: *gjr@cuk.ac.in*

3) Dr. Hussain Basha
Position: *Assistant Professor (Contractual),*
Address: *Department of Mathematics, Central University of Karnataka, Kalaburagi, India.*
Email: *hussainbmaths@gmail.com*

4) Dr. N. S. V. Narayanan
Position: *Assistant Professor,*
Address: *Department of Chemistry, Central University of Karnataka, Kalaburagi, India.*
Email: *nsvenkat@gmail.com*

5) Prof. O. Anwar Bég
Position: *Professor,*
Address: *Multi-physical Engineering Sciences, Aeronautical/Mechanical Engineering Department, School of Science, Engineering and Environment, Salford University, Manchester M54WT, UK.*
Email: *O.A.Beg@salford.ac.uk*

Abstract

The current study investigates the supercritical convective radiative buoyancy-driven flow and heat transfer in external coating flow of an electrically conducting viscoelastic thirdgrade nanofluid from hotmoving /stationary cylinderunder constant radial magnetic field. A new computational thermodynamic model has been proposedto study the supercritical behaviour of thirdgrade aqueous nanofluid in terms of supercritical water (SCW). The Redlich–Kwong equation of state (RK-EOS) has been deployed to calculatethermal expansion coefficient for free convective flow of supercritical nanofluid in terms of temperature, compressibility factor and pressure. A validation test has been conducted for RK-EOS with available experimental results. A well-tested conditionally stable Crank-Nicolson finite difference scheme has been implemented to obtain numerical solutions for the transformed dimensionless coupledconservation equations.Graphical results for flow variables, heat transfer and skin-friction coefficient distributions are presented for variation of Nanoscale, rheological, magnetic, radiative and thermodynamic parameters. Transient velocity is reduced whereas temperature is elevated with amplified values of third-grade fluid parameter, reduced pressure, reduced temperature, and decreased values of volume fraction of nanofluid for a stationary cylinder under supercritical conditions. Validation of special cases of the model computed with the Crank Nicolson method is conducted against previously published results. Important applications of the current study include nuclear reactor vessels, deposition of smart (functional magnetic) nano-coatings and solar collector energy systems.

Keywords:*Supercritical water, third grade nanofluid, RK-EOS thermodynamics, reduced temperature, vertical stationary/moving cylinder, magnetic field, thermal radiation.*

Nomenclature

Ag silver nanoparticles

g' acceleration due to gravity

N thermal radiation parameter

Gr Grashof number

M_0 strength of magnetic field

Pr Prandtl number

C_p specific heat at constant pressure

q_r radiative heat flux

$\overline{C_f}$ dimensionless skin friction coefficient

$\overline{Nu}$ average heat rate

I identity tensor

Nu_X local Nusselt number

V molar volume

Ra_X local Rayleigh number

R' universal gas constant

Z compressibility factor

k thermal conductivity

r_o radius of the cylinder

d diameter of cylinder

t' time

t dimensionless time

T' temperature

P fluid pressure

T dimensionless temperature

T^{**} matrix transposition

S_1', S_2', S_3' Rivlin and Ericksen tensors

$\frac{d}{dt}$ material time derivative

T_r^* reduced temperature

tr trace

P_r^* reduced pressure

r radial coordinate

x axial coordinate

u, v velocity components in x and r–directions, respectively

X non-dimensional axial coordinate

R non-dimensional radial coordinate

U, V non-dimensional velocity components (X, R) coordinates.

Greek letters

$\alpha_1', \alpha_2', \beta_1', \beta_2', \beta_3'$ rheological material moduli

σ electrical conductivity

β non-dimensional third-grade fluid parameter

β_T thermal expansion coefficient

τ' Cauchy stress tensor

ρ density

φ volume fraction of nanoparticles

μ dynamic viscosity

ρ^* ideal gas density

ϑ kinematic viscosity

σ^* Stefan-Boltzmann constant

κ^* mean absorption coefficient

Subscripts

nf nanofluid

bf base fluid

s solid nanoparticles

w wall conditions

c critical condition

r reduced characteristics

f, g grid levels in (X, R) coordinate system

∞ ambient conditions

Superscripts

h time level

1. Introduction

The demand of high pressurized steam in many industrial applications has motivated significant activity to optimize the design of higher capacity steam generators which can sustain the associated supercritical pressure. All heat transfer devices are designed such that the temperature of the super-heated tubes should not exceed the limitations enforced by structural strength of the materials. Nuclear power plants are also being designed to withstand the supercritical pressures. To overcome all these challenges, the designer should keep all these factors in mind to achieve sustained performance and the best service. Along with this, how nuclear reactor systems for example can be cooled safely is intimately linked to the efficiency of power generators and can critically simplify associatedpower plant systems. In this regard, the study of supercritical fluids (SCF) plays a crucial role.

Providing improved cooling technology is an essential need in many modern heat transfer applications such as combustion chambers, advanced gas turbine engines, power-generation systems and many. This process of cooling generally takes place at a pressure greater than the critical pressure of the coolant (such as engine fuel), hence resulting in the heat transfer. When the fluid operates *above* its critical temperature and pressure, it starts to exhibit supercritical properties i.e., vapor-like viscosity and liquid-like density. A very minor variation in temperature or pressure can significantly change the thermo-physical properties of the fluid and may improve the heat transfer characteristics considerably. Supercritical fluids arealso ecologically acceptable, biocompatible and a pragmatic substitute for conventionalsolvents. Furthermore, supercritical fluids can result in reactions which are challenging to achieve with conventional solvents. Supercritical fluids can act as a *medium for extraction*, as they promote speedy extraction owing to low viscosities and high diffusivities. Thereexcellent solvent characteristics make them efficient in chemical/petroleum engineering extraction processes, reaction systems and in chromatography. The use of supercritical fluids also features in cosmetics, pharmaceutics (purifying chemical compounds and synthesizing nanoparticles for biomedicine), catalytic chemistry, materials, drug delivery, power engineering, food manufacture, aerospace engineering, energy and waste management.Comprehensive studies on characteristics of many supercritical fluids and their applications along with supercritical water can be found in previous literature [1-11]. Many researchers have given thorough details on the thermodynamic characteristics of SCFs[12-14].

Among many energy resources, *nuclear energy* is relatively safe, extremely efficient, clean and sustainable energy resource and presently the only feasible substitute for conventional fossil fuel. Hence, it can satisfy worldwide energy demands. In this respect, the safety of these plants, utilization of produced energy and management of radioactive wastage are significant challenges. To achieve the requirements of sustainable green technology, the supercritical pressure water-cooled reactor (SCWR) plays a prominent role. In the management of industrial waste, supercritical water has been used to eradicate poisonous substances and aqueous toxins by the method of supercritical water oxidation (SCWO). Also, one can find numerous industrial fluid phenomena which operate at supercritical temperatures and pressurese.g., supercritical water fluidized bed reactor (SCWFBR), supercritical water biomass valorization (SCBV), supercritical pressure water-cooled reactor (SCWR), supercritical fluid extraction (SFE),power engineering, etc. There are many experimental studies on supercritical water addressing diverse applications in technology [15-23]. In view of this, interest in continued computational investigations of supercritical water transport phenomena is understandably high and the motivation for the present article.

Detailed knowledge of thermal science is necessary to enhance the thermal efficiency of heating equipment, via cost savings andoptimized materials, in addition to substantial reduction of ecological degradation. These factors have mobilized the advancementof heating techniques and increasingly more efficient techniques for heat transfer.The improvements in heat transfer devices are made possible via minimizing thermal resistanceand stimulating higher coefficients of heat transfer. In this regard, nanomaterials technology is a great platform for achieving high heat transfer devices. The suspensions of nanoparticles in base working fluids (i.e., nanofluids) have been confirmed widely to achieve crucial enhancement in heat transfer performance in for exampleautomotive/aerospace transportation, industrial heating/cooling appliances, heat exchangers, petroleum recovery, nuclear power plants, granular and fiber insulation,catalytic reactors, nuclear waste depositories, and biomedical applications such as wound healing, drug delivery, tissue engineering, hemodynamics etc. Nanofluids are Nanoscale-engineered heat conducting thermo-fluidswhich comprisea base fluid (with low thermal conductivity) and suspended nano-size particles (solid particles show better thermal performance). The size, shape, type and volume fraction of nanoparticles in base fluid contribute significantly in modifying the thermophysical characteristics of nanofluids. Micro-sized particles will have a tendency to settle down in suspensions under gravity resulting in blockage of pipes. These large-sized particles can cause corrosion and surficial damage to heat devices. Nano-sized metallic particles offer substantial advantages over micro-particlesowing to a range of excellent electronic, optical, chemical and thermo properties. Popular applications of nanofluids can be found in diagnostic biological probes, surface-enhanced Raman spectroscopy, microelectronics, catalysts, optoelectronics, photonics, optical sensors, solar collectors, rocket fuel, geological remediation and display devices. Choi [24] was the first to report the benefits of nanofluidsand demonstrated their superior thermal conductivity properties in automotive radiator cooling systems. Masuda et *al.* [25] and Eastman [26] also confirmed the considerable enhancement of thermal conductivity in nanofluids compared with base fluids. Higher thermal conductivity, critical heat flux and single phase heat transfer are promising characteristics of nanofluids which render them as excellent coolants [27] and [28].

Another group of nanofluids are *electromagnetic nanofluids*. These impart functionality to the nanofluid and make it responsive to external electrical and magnetic fields. The flow of an electrically conducting nanofluid over a vertical cylinder has many technical and industrial applications such asbiological coatings, micro-mixing of physiological samples, high-temperature plasma deposition, MHD micro pump surface lining and drug coatings. Magnetic nanofluids also have applications as magneto-gravimetric separation media, aerodynamic sensors, leakage-free magneto-fluidic rotating seals, semi-active smart vibration dampers, inclinations/acceleration sensors, biomedical applications,gastric medications, sterilized devicesand in plant genetics. The magneto nanoparticles considerably used in tumor analysis, cancer therapy, magneto-acoustic loud-speaker designs, sink float separation etc.Thumma *et al*. [29] used a variational finite element method to compute viscous heating effects in magnetic nanofluid boundary layer flow from a tilted expanding/contracting surface using the Buongiorno Nanoscale model for materials processing systems. Bég*et al.* [30] investigated multiple metallic nanoparticle effects (silver, titanium, aluminium etc) in transport modelling of magnetic functional solar nanofluid coating enrobing flows with a Tiwari-Das model and MATLAB quadrature. Hayat *et al.* [31] computed the magnetic mixed-convective peristaltic flow of nanofluid with Soret and Dufour effects. Prakash *et al.*[32] worked on magnetized nanofluid dynamics in bio inspired smart pumps using integral and finite difference methods. Some of the recent studies on nanofluid are mentioned [77-80, 82].

We can find many studies which are reported on thenon-Newtonian characteristics of nanofluidsassociated with the occurrence of nanoparticle clusters e. g. stress relaxation, normal stress differences, variation in the viscosity, non-linearity of creeping, threshold stress, viscosity depending on temperature, shear thinning/thickening and memory fluid behavior. Many experimental and theoretical studies have supported this non-linear behavior of nanofluids. Suspension of nano-sized particles inconventional base fluid or base fluid itself contributes to a modification in the rheology and leads to non-Newtonian behavior of nanofluids under different shear rate conditions([70], [71], [72] [74], [75] and [81]).Tseng and Chen [33] have demonstrated the pseudoplastic nature of nanofluid (suspensions of nickel-terpineol) experimentally. The experimental study of Kathy Lu [34] showed the shear thinning property of nanofluid with variation in rate of shear. Phuoc and Massoudi [35]observed viscoplastic non-Newtonian behavior (yield stress) in nanofluids. An experimental justification has been given by Chen *et al.* [36] relating to nanofluid dependence on temperature and concentration and this also constitutes a non-Newtonian property.To study thermo-fluid behaviour of real nanofluids, it is necessary to adopt robust '*non-Newtonian theory*' in conjunction with an appropriate '*Nanoscale fluid model*'.Chemical engineers and polymer physicists have developed a wide range of comprehensive rheological fluid models e. g. integral, rate and differential type non-Newtonian models. These can be utilized also to elucidate the non-linear shear stress-strain behaviour in nanofluids. The *viscoelastic third-grade fluid model* is another thermodynamically rigorous formulation which belongs to the Reiner-Rivlin subclass of differential type of fluids, that are known to exhibit relationships between the stress history and deformation gradient. This model also simulates quite accurately the shear thickening (dilatant) and shear-thinning (pseudoplastic) features observed in nanofluid suspensions. The third-grade model satisfactorily captures the real characteristics of slurries, physiological liquids, polymer/aqueous coatings, certain coolants and lubricants.Significant theoretical and numerical research has been published in particular relating to convective heat transfer of third-grade fluid flows [37-43, 73] owing to applications in thermal polymer coating technologies.Third-grade rheological nanofluid flows have more recently stimulated some attention in applied mechanics and engineering sciences. Hiremath *et al.* [44] investigated the thirdgrade nanofluid boundary layer flow from a convectivelyheated vertical cylinder, reporting in detail on heat transfer characteristics.The dissipative two-layer buoyancy-driven channel flow of thirdgrade nanofluid was investigated by Farooq *et al.* [45]. Nadeem and Saleem [46] computed the nanofluid third grade convection from a spinning upright vertical cone with wall effects.Further contributions on thirdgrade nanofluid simulations are listed in the references [47-49].

The present study aims to consider the magnetohydrodynamic (MHD) and thermal radiation effects on thirdgrade nanofluid flow and heat transfer from vertically heated stationary/moving cylinder under supercritical conditions. Magnetic effects can be invoked by the electromagnetic properties of nanoparticles. Radiative heat transfer is considered due to the high temperature conditions common in thermal nano-coating operation. This investigation considerssilver (*Ag*) nano particles and supercritical water as the base fluid. The normalized partial differential equations for mass, momentum and energy conservation with supercritical thermodynamic modifications are solved with a stable, efficient implicit Crank-Nicolson*finite difference procedure*. Steady and unsteady flow characteristics of the regime are computed including heat transfer coefficient and skin friction coefficient. Comprehensive visualization of solutions is included as are validations with previous simpler models in the literature. The numerical simulations provide an important compliment to experimental studies and furthermore furnish a good benchmark for future extensions of the study.

2. Equation for β_T in SCF region based on RK-EOS

Many free convective heat transfer flow problems at supercritical conditions consider theβ_T (thermal expansion coefficient) to be constant with Boussinesq's approximation and a limitation of this approach is that thermal expansion coefficientvariation with pressure and temperature is neglected. In the supercritical region, these considerations may contribute unacceptable inaccuracy in the results, since thermal expansion coefficient (β_T) among all the properties of fluid is sensitive to pressure and temperature variations(refer **Fig. 1**). For that reason, it is very important to select asuitable equation of state (EOS) for deriving the equation to calculate

β_T values.Therefore RK-EOS [50] is chosen as the EOS in the current study and $\beta_T$has been calculated as being a function of temperature (T'), pressure (P) and compressibility factor (Z).

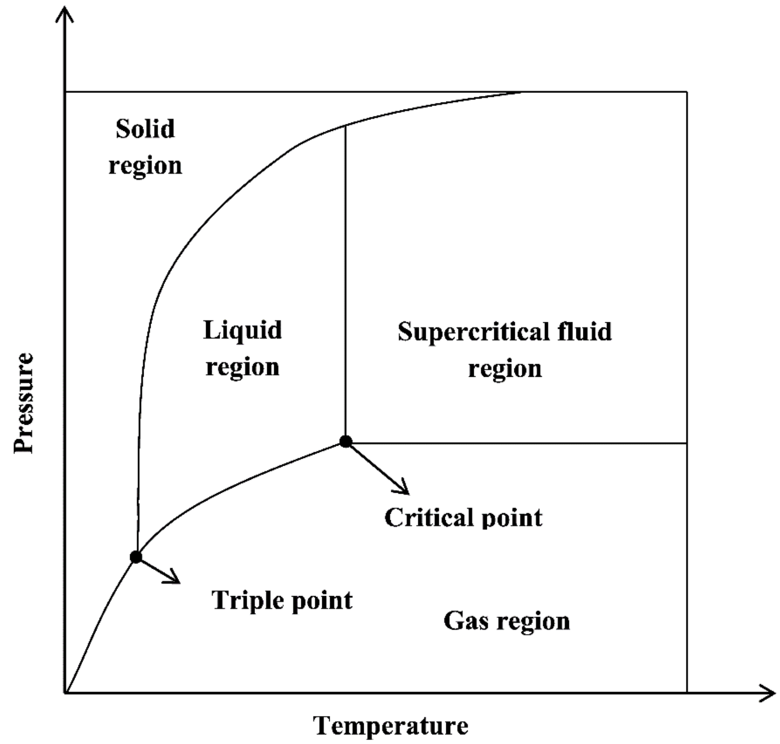

Fig. 1.Idealized phase diagram of the supercritical nanofluid

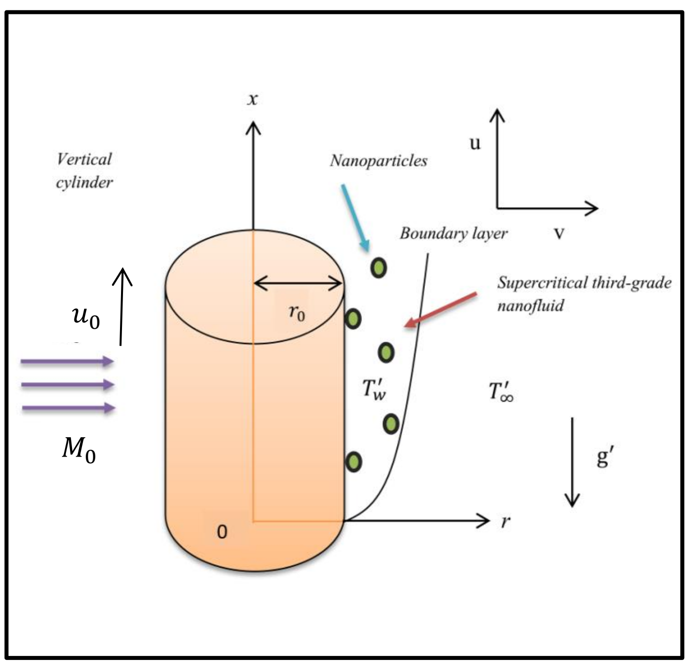

Fig. 2 Physical representation of the current magnetic nano-coating problem.

For fixed pressure value, $\beta_T = -\frac{1}{\rho}\left(\frac{\partial \rho}{\partial T'}\right)_P$. For gases at different P and T' values,the RK-EOS is given by $P = \frac{R'T'}{V'-b} - \frac{a}{\sqrt{T'}(V'(V'+b))}$(where a and b are RK-EOS constantsevaluated forcritical point properties). Also, the expression for$Z$based on theRK-EOS - see [51]- is:

$$Z^3 - Z^2 + \left(A' - B' - B'^2\right)Z - A'B' = 0 \qquad (1)$$

where $A' = \frac{aP}{\sqrt{T'}(R'T')^2}$, $Z = \frac{PV'}{R'T'}$, $B' = \frac{bP}{R'T'}$

At the defined T_c (critical temperature)= 647.30K andP_c (critical pressure)= 22.090MPa, RK-EOS gives the constant values as :$A' = 0.42748\left(\frac{P}{P_c}\right)\left(\frac{T_c}{T'}\right)^{2.5}$and $B' = 0.08662\left(\frac{P}{P_c}\right)\left(\frac{T_c}{T'}\right)$. Finally, the expression for$\beta_T$is defined as follows:

$$\beta_T = \frac{1}{T'}\left[1 - \left(\frac{3.5A'B' + 2ZB'^2 + B'Z - 2.5A'Z}{3Z^3 - 2Z^2 + Z(A' - B') - B'^2 Z}\right)\right] \qquad (2)$$

Subsequently, β_T can be expressedby considering Van der Waals equation of state (VW-EOS) [52] as:

$$\beta_T = \frac{1}{T'}\left[1 - \left(\frac{Z^2B' - 2ZA' + 3A'B'}{3Z^3 - 2Z^2(B'+1) + A'Z}\right)\right] \qquad (3)$$

Thus, the$\beta_T$is calculated in a *two-step process*. Initially, Z from Eq. (1) is calculated. Later,$\beta_T$is evaluated by virtue of Eqns. (2) and (3) with the earlier calculated Z value.

3. Supercritical magnetic nanofluid third-grade flow coating model

The current mathematical model considers the study of electrically conducting supercritical viscoelastic thirdgrade nanofluid over a semi-infinite moving cylinder (radius r_o) which is directed vertically with constant strength, static magnetic field M_0 in the*r*- direction. The cylinder is subjected to a radial radiative heat flux, q_r. A fixed rectangular coordinate system is employed. The axis of the cylinder is orientated along the *x*-direction and *r*-coordinate is aligned along the radial direction (refer**Fig. 2**). Magnetic induction is neglected owing to small magnetic Reynolds numbers as is Ohmic magnetic heating (Joule dissipation). At starting time $t' = 0$, T'_∞ is the constant temperature in the free-stream external to the boundary layer regime on the cylinder and of the rheological nanofluid. Later as time progress $(t' > 0)$, the cylinder starts to move with constant velocity $u_0$in the vertically upward direction and attains a temperature T'_w. Thereafter this same temperature (T'_w) is sustained. The nanofluid non-Newtonian behaviour is simulated with the third-grade fluid model (as the base fluid) and homogenously distributed silver (*Ag*) nanoparticles are assumed to be in a dilute state of local thermal equilibrium.The considered supercritical nanofluid in this study is assumed to be *a single-phase* fluid in the SCF region. In addition to this, the no-slip condition is also enforced at the cylinder surface. The thermophysical properties of base fluid and nanoparticles are shown in the **Table 1**([53] and [54]). The "Cauchy's stress-tensor (τ')" for the non-Newtonianthird-grade fluid (Fosdick and Rajagopal [55]) takes the form:

$$\tau' = -PI + \mu S'_1 + \alpha'_1 S'_2 + \alpha'_2 {S'_1}^2 + \beta'_1 S'_3 + \beta'_2 (S'_1 S'_2 + S'_2 S'_1) + \beta'_3 (tr {S'_1}^2) S'_1 \qquad (4)$$

Here $\alpha'_l (l = 1,2)$ and $\beta'_l (l = 1,2,3)$ are temperature-dependent *material moduli*, $-PI$signifies the spherical portion of τ'(stress-tensor), and S'_l $(l = 1,2,3)$ are '*Rivlin-Erickson tensor matrices'* represented through Eq. (5):

$$S'_1 = (\nabla \boldsymbol{V})^{T^{**}} + \nabla \boldsymbol{V} \ , S'_l = \frac{dS'_{l-1}}{dt} + (\nabla \boldsymbol{V})^{T^{**}} S'_{l-1} + S'_{l-1}(\nabla \boldsymbol{V}), \ \ l = 2,3 \ldots. \qquad (5)$$

$\frac{d}{dt}$ is known as the *material derivative* where $\frac{d}{dt}(\cdot) = \left(\frac{\partial}{\partial t} + \boldsymbol{V}\nabla\right)(\cdot)$.The transpose of matrix, velocity vector and gradient operator are symbolized as T^{**}, $\boldsymbol{V}$and ∇respectively. The inequality defined by '*Clausius-Duhem*' and the least feasible value of '*Helmholtz free-energy*' at the state of equilibrium are the minimum thermodynamic principles to be satisfied by the third-grade model. Hence, third-grade fluid model follows the following constraints:

$\mu \geq 0; \quad \alpha_1' \geq 0; \quad |\alpha_1' + \alpha_2'| \leq \sqrt{24\mu\beta_3'}$(6.a)

$\beta_1' = 0; \quad \beta_2' = 0; \quad \beta_3' \geq 0$(6.b)

Eqn. (4) thereby leads to:

$\tau' = -PI + \mu S_1' + \alpha_1' S_2' + \alpha_2' {S_1'}^2 + \beta_3'(tr{S_1'}^2)S_1'$(7)

This axisymmetric thermally convective flow of magnetized non-Newtonian viscoelastic third-grade nanofluid in the presence of '*transverse magnetic field* (M_0)' from a moving vertical cylinder (velocity u_0) may then bedescribed by the subsequent mass, momentum and energy (heat) conservationboundary layer equations [56] with the Boussinesq approximation [57] with thermal radiation contribution expressedfollowing [39], [40], [44] & [58] (visualized in **Fig. 2**):

$$\frac{\partial(ru)}{\partial x} + \frac{\partial(rv)}{\partial r} = 0 \tag{8}$$

$$\begin{aligned}\frac{\partial u}{\partial t'} + v\frac{\partial u}{\partial r} + u\frac{\partial u}{\partial x} = \frac{(\rho\beta_T)_{nf}}{\rho_{nf}} g'(T' - T'_\infty) + \vartheta_{nf}\frac{1}{r}\frac{\partial}{\partial r}\left(r\frac{\partial u}{\partial r}\right) + \frac{\alpha_1'}{\rho_{nf}}\left[\frac{\partial^3 u}{\partial r^2 \partial t'} + \frac{1}{r}\frac{\partial^2 u}{\partial r \partial t'} + v\frac{\partial^3 u}{\partial r^3}\right.\\ +2\frac{\partial v}{\partial r}\frac{\partial^2 u}{\partial r^2} + 3\frac{\partial^2 u}{\partial r^2}\frac{\partial u}{\partial x} + \frac{\partial u}{\partial r}\frac{\partial^2 v}{\partial r^2} + 4\frac{\partial u}{\partial r}\frac{\partial^2 u}{\partial x \partial r} + \frac{v}{r}\frac{\partial^2 u}{\partial r^2} + \frac{u}{r}\frac{\partial^2 u}{\partial x \partial r} +\\ \left.\frac{3}{r}\frac{\partial u}{\partial x}\frac{\partial u}{\partial r} + u\frac{\partial^3 u}{\partial x \partial r^2} + \frac{1}{r}\frac{\partial u}{\partial r}\frac{\partial v}{\partial r}\right] + \frac{\alpha_2'}{\rho_{nf}}\left[\frac{2}{r}\frac{\partial u}{\partial r}\frac{\partial v}{\partial r} + \frac{2}{r}\frac{\partial u}{\partial x}\frac{\partial u}{\partial r} + 2\frac{\partial^2 u}{\partial r^2}\frac{\partial u}{\partial x} +\right.\\ \left.+2\frac{\partial^2 v}{\partial r^2}\frac{\partial u}{\partial r} + 2\frac{\partial v}{\partial r}\frac{\partial^2 u}{\partial r^2} + 4\frac{\partial u}{\partial r}\frac{\partial^2 u}{\partial x \partial r}\right] + \frac{\beta_3'}{\rho_{nf}}\left[\frac{2}{r}\left(\frac{\partial u}{\partial r}\right)^3 + 6\left(\frac{\partial u}{\partial r}\right)^2\frac{\partial^2 u}{\partial r^2} +\right.\\ \left.4\left(\frac{\partial u}{\partial r}\right)^2\frac{\partial^2 u}{\partial x^2} + 2\frac{\partial u}{\partial x}\frac{\partial u}{\partial r}\frac{\partial^2 u}{\partial x \partial r}\right] - \frac{\sigma M_0^2 u}{\rho_{nf}}\end{aligned} \tag{9}$$

$$\frac{\partial T'}{\partial t'} + u\frac{\partial T'}{\partial x} + v\frac{\partial T'}{\partial r} = \frac{k_{nf}}{(\rho C_p)_{nf}}\frac{1}{r}\frac{\partial}{\partial r}\left(r\frac{\partial T'}{\partial r}\right) - \frac{1}{(\rho C_p)_{nf}}\frac{1}{r}\frac{\partial}{\partial r}(rq_r) \tag{10}$$

Here(u, v) denote the axial and transverse (radial) velocity components along (x, r) coordinates.

The appropriate initial and boundary conditions are as follows:

$t' \leq 0$: $T' = T'_\infty$, $v = 0$, $u = 0$ for all x and r

$t' > 0$: $T' = T'_w$, $v = 0$, $u = \lambda u_0$ at $r = r_0$

$T' = T'_\infty$, $v = 0$, $u = 0$ at$x = 0$

$T' \to T'_\infty$, $v \to 0$, $u \to 0, \frac{\partial u}{\partial r} \to 0asr \to \infty$

(11)The density, thermal expansion coefficient and heat capacitance for nanofluid are calculated using

$$\rho_{nf} = (1 - \varphi)\rho_{bf} + \varphi\rho_s$$

$$(\rho\beta_T)_{nf} = (1 - \varphi)(\rho\beta_T)_{bf} + \varphi(\rho\beta_T)_s \quad (12)$$

$$\left(\rho C_p\right)_{nf} = (1 - \varphi)\left(\rho C_p\right)_{bf} + \varphi\left(\rho C_p\right)_s$$

Also, thermal conductivity of nanofluid is considered based on the Hamilton-Crosser model [59] i.e.,

$$\frac{k_{nf}}{k_{bf}} = \frac{k_s + (n-1)k_{bf} - (n-1)\varphi\left(k_{bf} - k_s\right)}{k_s + (n-1)k_{bf} + \varphi\left(k_{bf} - k_s\right)} \quad (13)$$

Here n defines the shape of nanoparticles.Precisely, $n = 3$ & $3/2$ indicates spherical and cylindrical, respectively (details can be found in **Table. 2**[53]).

By assuming the ‘Rosseland thermal radiation approximation’ (Brewster [60]), the radiative heat flux q_r is expressed as:

$$q_r = -\frac{4\sigma^*}{3\kappa^*}\frac{\partial T'^4}{\partial r} \quad (14)$$

For adequately small temperature differences within the fluid flow, the term, T'^4may be conveyed as a linear function of the temperature, so that the Taylor series for T'^4 about T'_∞, after ignoring higher order terms, is specified by the following equation:

$$T'^4 \cong 4T'T'^3_\infty - 3T'^4_\infty \quad (15)$$

From Eqns. (14) & (15), Eqn. (10) implies that,

$$\frac{\partial T'}{\partial t'} + u\frac{\partial T'}{\partial x} + v\frac{\partial T'}{\partial r} = \frac{k_{nf}}{(\rho C_p)_{nf}}\frac{1}{r}\frac{\partial}{\partial r}\left(r\frac{\partial T'}{\partial r}\right) + \frac{16\sigma^* {T'}_{\infty}^{3}}{3(\rho C_p)_{nf}\kappa^*}\frac{1}{r}\frac{\partial}{\partial r}\left(r\frac{\partial T'}{\partial r}\right) \quad (16)$$

Introducing the subsequent non-dimensional quantities:

$$X = \frac{x\vartheta_{bf}}{u_0{r_0}^2}, \qquad R = \frac{r}{r_0}, \qquad U = \frac{u}{u_0}, \qquad V = \frac{vr_0}{\vartheta_{bf}}, t = \frac{t'\vartheta_{bf}}{{r_0}^2},$$

$$T = \frac{T' - T'_\infty}{T'_w - T'_\infty}, \quad Gr = \frac{g'(\beta_T)_{bf}{r_0}^2(T'_w - T'_\infty)}{u_0\vartheta_{bf}}, \quad Pr = \frac{\vartheta_{bf}}{\alpha_{bf}}, \quad M = \frac{\sigma M_0^2 r_0^2}{\mu_{bf}}, \quad N = \frac{k_{bf}\kappa^*}{4\sigma^* {T'}_\infty^3}$$

$$\alpha_1 = \frac{\alpha'_1}{\rho_{bf}{r_0}^2}, \qquad \alpha_2 = \frac{\alpha'_2}{\rho_{bf}{r_0}^2}, \qquad \beta = \frac{\beta'_3\, u_0^2}{\rho_{bf}{r_0}^2\vartheta_{bf}}, \quad \beta' = \frac{\beta'_3\,\vartheta_{bf}}{\rho_{bf}{r_0}^4} \quad (17)$$

Implementing Eqn. (17) in the conservation Eqns. (8), (9), (16) and Eqn. (11), the following system of non-dimensional governing equations emerge:

$$\frac{\partial U}{\partial X} + \frac{\partial V}{\partial R} + \frac{V}{R} = 0 \qquad (18)$$

$$\begin{aligned} U\frac{\partial U}{\partial X} + V\frac{\partial U}{\partial R} + \frac{\partial U}{\partial t} &= AC(Gr)T + AB\frac{1}{R}\frac{\partial}{\partial R}\left(R\frac{\partial U}{\partial R}\right) \\ &+ A\alpha_1\left[\frac{\partial^3 U}{\partial R^2\partial t} + \frac{1}{R}\frac{\partial^2 U}{\partial R\partial t} + U\frac{\partial^3 U}{\partial X\partial R^2} + V\frac{\partial^3 U}{\partial R^3} + \frac{U}{R}\frac{\partial^2 U}{\partial X\partial R} + \frac{V}{R}\frac{\partial^2 U}{\partial R^2}\right. \\ &\left. + 2\frac{\partial V}{\partial R}\frac{\partial^2 U}{\partial R^2} + 3\frac{\partial^2 U}{\partial R^2}\frac{\partial U}{\partial X} + \frac{\partial U}{\partial R}\frac{\partial^2 V}{\partial R^2} + 4\frac{\partial U}{\partial R}\frac{\partial^2 U}{\partial X\partial R} + \frac{1}{R}\frac{\partial U}{\partial R}\frac{\partial V}{\partial R} + \frac{3}{R}\frac{\partial U}{\partial X}\frac{\partial U}{\partial R}\right] \\ &+ A\alpha_2\left[\frac{2}{R}\frac{\partial U}{\partial R}\left(\frac{\partial V}{\partial R} + \frac{\partial U}{\partial X}\right) + 2\frac{\partial^2 U}{\partial R^2}\left(\frac{\partial U}{\partial X} + \frac{\partial V}{\partial R}\right) + 2\frac{\partial U}{\partial R}\left(\frac{\partial^2 V}{\partial R^2} + 2\frac{\partial^2 U}{\partial X\partial R}\right)\right] \end{aligned}$$

$$+ A\beta\left[\frac{2}{R}\left(\frac{\partial U}{\partial R}\right)^3 + 6\frac{\partial^2 U}{\partial R^2}\left(\frac{\partial U}{\partial R}\right)^2\right] + A\beta'\left[4\frac{\partial^2 U}{\partial X^2}\left(\frac{\partial U}{\partial R}\right)^2 + 2\frac{\partial^2 U}{\partial X\partial R}\frac{\partial U}{\partial X}\frac{\partial U}{\partial R}\right] - AMU \quad (19)$$

$$U\frac{\partial T}{\partial X} + V\frac{\partial T}{\partial R} + \frac{\partial T}{\partial t} = \frac{D}{Pr}\left(E + \frac{4}{3N}\right)\left(\frac{\partial^2 T}{\partial R^2} + \frac{1}{R}\frac{\partial T}{\partial R}\right) \qquad (20)$$

$t \leq 0$: $T = 0$, $V = 0$, $U = 0$ for all$X$and$R$

$t > 0$: $T = 1$, $V = 0$, $U = \lambda$at$R = 1$

$T = 0$, $V = 0$, $U = 0$ at$X = 0$ (21)

$T \to 0$, $V \to 0$, $U \to 0$, $\frac{\partial U}{\partial R} \to 0asR \to \infty$

where

$$A = \frac{1}{\left[(1-\varphi)+\varphi\frac{\rho_s}{\rho_{bf}}\right]}, B = \frac{1}{(1-\varphi)^{2.5}}, C = \left[(1-\varphi) + \varphi\frac{(\rho\beta_T)_s}{(\rho\beta_T)_{bf}}\right], D = \frac{1}{\left[(1-\varphi)+\varphi\frac{(\rho C_p)_s}{(\rho C_p)_{bf}}\right]}, E = \frac{k_{nf}}{k_{bf}} \quad (22)$$

4. Finite difference numerical solution

Eqns. (18) - (21) are a nonlinear, coupled dimensionless system of boundary layer flow equations which cannot be solved with analytical procedures. However, there are certain numerical procedures which provide a solution with greater accuracy. The implicit finite difference scheme (i.e., *Crank-Nicolson type*[61]) with*unconditionally stable*property is employed.The discretized finite difference equations for Eqns. (18) to (20)assume the form:

$$\frac{U_{f,g}^{h+1} - U_{f-1,g}^{h+1} + U_{f,g}^{h} - U_{f-1,g}^{h}}{2\Delta X} + \frac{V_{f,g}^{h+1} - V_{f,g-1}^{h+1} + V_{f,g}^{h} - V_{f,g-1}^{h}}{2\Delta R} + V_{f,g}^{h+1}(JR) = 0 \quad (23)$$

$$\frac{U_{f,g}^{h+1} - U_{f,g}^{h}}{\Delta t} + U_{f,g}^{h}\frac{\left(U_{f,g}^{h+1} - U_{f-1,g}^{h+1} + U_{f,g}^{h} - U_{f-1,g}^{h}\right)}{2\Delta X} + V_{f,g}^{h}\frac{\left(U_{f,g+1}^{h+1} - U_{f,g-1}^{h+1} + U_{f,g+1}^{h} - U_{f,g-1}^{h}\right)}{4\Delta R}$$

$$= AC(Gr)\frac{T_{f,g}^{h} + T_{f,g}^{h+1}}{2} + AB\frac{JR}{4\Delta R}\left(U_{f,g+1}^{h+1} - U_{f,g-1}^{h+1} + U_{f,g+1}^{h} - U_{f,g-1}^{h}\right)$$

$$+AB\frac{1}{2(\Delta R)^2}\left(U_{f,g-1}^{h+1} - 2U_{f,g}^{h+1} + U_{f,g+1}^{h+1} + U_{f,g-1}^{h} - 2U_{f,g}^{h} + U_{f,g+1}^{h}\right)$$

$$+\mathrm{A}\alpha_1\left[\frac{1}{4(\Delta R)^2(\Delta t)}\left(U_{f,g-2}^{h+1}-2U_{f,g}^{h+1}+U_{f,g+2}^{h+1}-U_{f,g-2}^{h}+2U_{f,g}^{h}-U_{f,g+2}^{h}\right)\right.$$

$$+\frac{JR}{2(\Delta R)(\Delta t)}\left(U_{f,g+1}^{h+1}-U_{f,g-1}^{h+1}-U_{f,g+1}^{h}+U_{f,g-1}^{h}\right)$$

$$+\frac{V_{f,g}^{h}}{4(\Delta R)^3}\left(U_{f,g+2}^{h+1}-2U_{f,g+1}^{h+1}+2U_{f,g-1}^{h+1}-U_{f,g-2}^{h+1}+U_{f,g+2}^{h}-2U_{f,g+1}^{h}\right.$$

$$\left.+2U_{f,g-1}^{h}-U_{f,g-2}^{h}\right)$$

$$+\frac{1}{2(\Delta R)^3}\left(V_{f,g+1}^{h}-V_{f,g-1}^{h}\right)\left(U_{f,g-1}^{h+1}-2U_{f,g}^{h+1}+U_{f,g+1}^{h+1}+U_{f,g-1}^{h}-2U_{f,g}^{h}\right.$$

$$\left.+U_{f,g+1}^{h}\right)$$

$$+\frac{3}{2(\Delta X)(\Delta R)^2}\left(U_{f,g}^{h}-U_{f-1,g}^{h}\right)\left(U_{f,g-1}^{h+1}-2U_{f,g}^{h+1}+U_{f,g+1}^{h+1}+U_{f,g-1}^{h}-2U_{f,g}^{h}\right.$$

$$\left.+U_{f,g+1}^{h}\right)$$

$$+\frac{1}{4(\Delta R)^3}\left(U_{f,g+1}^{h+1}-U_{f,g-1}^{h+1}+U_{f,g+1}^{h}-U_{f,g-1}^{h}\right)\left(V_{f,g-1}^{h}-2V_{f,g}^{h}+V_{f,g+1}^{h}\right)$$

$$+\frac{1}{2(\Delta X)(\Delta R)^2}\left(U_{f,g+1}^{h}-U_{f,g-1}^{h}\right)\left(U_{f,g+1}^{h+1}-U_{f-1,g+1}^{h+1}-U_{f,g-1}^{h+1}+U_{f-1,g-1}^{h+1}+U_{f,g+1}^{h}-U_{f-1,g+1}^{h}\right.$$

$$\left.-U_{f,g-1}^{h}+U_{f-1,g-1}^{h}\right)$$

$$+\frac{V_{f,g}^{h}JR}{2(\Delta R)^2}\left(U_{f,g-1}^{h+1}-2U_{f,g}^{h+1}+U_{f,g+1}^{h+1}+U_{f,g-1}^{h}-2U_{f,g}^{h}+U_{f,g+1}^{h}\right)$$

$$+\frac{U_{f,g}^{h}JR}{4(\Delta R)(\Delta X)}\left(U_{f,g+1}^{h+1}-U_{f-1,g+1}^{h+1}-U_{f,g-1}^{h+1}+U_{f-1,g-1}^{h+1}+U_{f,g+1}^{h}-U_{f-1,g+1}^{h}-U_{f,g-1}^{h}\right.$$

$$\left.+U_{f-1,g-1}^{h}\right)$$

$$+\frac{3JR}{4(\Delta R)(\Delta X)}\left(U_{f,g}^{h}-U_{f-1,g}^{h}\right)\left(U_{f,g+1}^{h+1}-U_{f,g-1}^{h+1}+U_{f,g+1}^{h}-U_{f,g-1}^{h}\right)$$

$$+\frac{JR}{8(\Delta R)^3}\left(V_{f,g+1}^{h}-V_{f,g-1}^{h}\right)\left(U_{f,g+1}^{h+1}-U_{f,g-1}^{h+1}+U_{f,g+1}^{h}-U_{f,g-1}^{h}\right)$$

$$+\frac{U_{f,g}^{h}}{2(\Delta R)^2\Delta X}\left(U_{f,g+1}^{h+1}-U_{f-1,g+1}^{h+1}-2U_{f,g}^{h+1}+2U_{f-1,g}^{h+1}+U_{f,g-1}^{h+1}-U_{f-1,g-1}^{h+1}\right.$$

$$+U_{f,g+1}^{h}-U_{f-1,g+1}^{h}-2U_{f,g}^{h}+2U_{f-1,g}^{h}+U_{f,g-1}^{h}-U_{f-1,g-1}^{h}\big)\big]$$

$$+\mathrm{A}\alpha_2\left[\frac{JR}{4(\Delta R)^2}\left(V_{f,g+1}^{h}-V_{f,g-1}^{h}\right)\left(U_{f,g+1}^{h+1}-U_{f,g-1}^{h+1}+U_{f,g+1}^{h}-U_{f,g-1}^{h}\right)\right.$$

$$+\frac{JR}{2(\Delta R)(\Delta X)}\left(U_{f,g}^{h}-U_{f-1,g}^{h}\right)\left(U_{f,g+1}^{h+1}-U_{f,g-1}^{h+1}+U_{f,g+1}^{h}-U_{f,g-1}^{h}\right)$$

$$+\frac{1}{(\Delta X)(\Delta R)^2}\left(U_{f,g}^{h}-U_{f-1,g}^{h}\right)\left(U_{f,g-1}^{h+1}-2U_{f,g}^{h+1}+U_{f,g+1}^{h+1}+U_{f,g-1}^{h}-2U_{f,g}^{h}+U_{f,g+1}^{h}\right)$$

$$+\frac{1}{2(\Delta R)^3}\left(V_{f,g-1}^{h}-2V_{f,g}^{h}+V_{f,g+1}^{h}\right)\left(U_{f,g+1}^{h+1}-U_{f,g-1}^{h+1}+U_{f,g+1}^{h}-U_{f,g-1}^{h}\right)$$

$$+\frac{1}{2(\Delta X)(\Delta R)^2}\left(U_{f,g+1}^{h}-U_{f,g-1}^{h}\right)\big(U_{f,g+1}^{h+1}-U_{f-1,g+1}^{h+1}-U_{f,g-1}^{h+1}+U_{f-1,g-1}^{h+1}$$

$$+U_{f,g+1}^{h}-U_{f-1,g+1}^{h}-U_{f,g-1}^{h}$$

$$+U_{f-1,g-1}^{h}\big)+\frac{1}{2(\Delta R)^3}\left(V_{f,g+1}^{h}-V_{f,g-1}^{h}\right)\big(U_{f,g-1}^{h+1}-2U_{f,g}^{h+1}+U_{f,g+1}^{h+1}+U_{f,g-1}^{h}$$

$$\left.-2U_{f,g}^{h}+U_{f,g+1}^{h}\big)\right]$$

$$++A\beta\left[(JR)\frac{\left(U_{f,g+1}^{h}-U_{f,g-1}^{h}\right)^3}{4(\Delta R)^3}\right.$$

$$\left.+3\frac{\left(U_{f,g+1}^{h}-U_{f,g-1}^{h}\right)^2}{4(\Delta R)^2}\frac{\left(U_{f,g-1}^{h+1}-2U_{f,g}^{h+1}+U_{f,g+1}^{h+1}+U_{f,g-1}^{h}-2U_{f,g}^{h}+U_{f,g+1}^{h}\right)}{(\Delta R)^2}\right]$$

$$+A\beta'\left[\frac{\left(U_{f,g+1}^{h}-U_{f,g-1}^{h}\right)^2}{(\Delta R)^2}\frac{\left(U_{f-1,g}^{h}-2U_{f,g}^{h}+U_{f+1,g}^{h}\right)}{(\Delta X)^2}+\frac{1}{8}\frac{\left(U_{f,g}^{h}-U_{f-1,g}^{h}\right)}{(\Delta X)}\frac{\left(U_{f,g+1}^{h}-U_{f,g-1}^{h}\right)}{(\Delta R)}\right.$$

$$\left.\frac{\left(U_{f,g+1}^{h+1}-U_{f-1,g+1}^{h+1}-U_{f,g-1}^{h+1}+U_{f-1,g-1}^{h+1}+U_{f,g+1}^{h}-U_{f-1,g+1}^{h}-U_{f,g-1}^{h}+U_{f-1,g-1}^{h}\right)}{(\Delta X)(\Delta R)}\right]-AM\left[\frac{U_{f,g}^{h}+U_{f,g}^{h+1}}{2}\right]$$

(24)

$$\frac{T_{f,g}^{h+1}-T_{f,g}^{h}}{\Delta t}+U_{f,g}^{h}\frac{\left(T_{f,g}^{h+1}-T_{f-1,g}^{h+1}+T_{f,g}^{h}-T_{f-1,g}^{h}\right)}{2\Delta X}+V_{f,g}^{h}\frac{\left(T_{f,g+1}^{h+1}-T_{f,g-1}^{h+1}+T_{f,g+1}^{h}-T_{f,g-1}^{h}\right)}{4\Delta R}$$

$$= \frac{D}{Pr}\left(E + \frac{4}{3Nr}\right)\left[\frac{\left(T_{f,g-1}^{h+1} - 2T_{f,g}^{h+1} + T_{f,g+1}^{h+1} + T_{f,g-1}^{h} - 2T_{f,g}^{h} + T_{f,g+1}^{h}\right)}{2(\Delta R)^2} + (JR)\frac{\left(T_{f,g+1}^{h+1} - T_{f,g-1}^{h+1} + T_{f,g+1}^{h} - T_{f,g-1}^{h}\right)}{4(\Delta R)}\right] \tag{25}$$

The considered flow region is defined by the limits:$X_{min} = 0, X_{max} = 1$, $R_{min} = 1$ and $R_{max} = 20$(whereR_{max} implies to $R = \infty$). The temperature Eqn. (25) and momentum Eqn. (24) are discretized for all internal mesh points (f, g) at specific 'f - level' can be reduced to 'tridiagonal' and 'penta-diagonal' systems of equations are given by equations (26) & (27), respectively:

$$A_1\delta_{f,g-1}^{h+1} + B_1\delta_{f,g}^{h+1} + C_1\delta_{f,g+1}^{h+1} = D_1 \tag{26}$$

$$A_2\Upsilon_{f,g-2}^{h+1} + B_2\Upsilon_{f,g-1}^{h+1} + C_2\Upsilon_{f,g}^{h+1} + D_2\Upsilon_{f,g+1}^{h+1} + E_2\Upsilon_{f,g+2}^{h+1} = F_2 \tag{27}$$

At the $(h+1)^{th}$level, 'tridiagonal' [61] and 'penta-diagonal' [62] algorithms are used to solve Eqns. (26) and (27). Here, δ&Υ represent T&U, respectively. Details on these algorithms can be found in [61], [62]. The computational technique initially determines a solution for the temperature field (solving Eqn. (25) for T) then followed by the velocity field (solving Eqn. (24) for U). The generated U & T values are used explicitly to calculate V from Eqn. (23).

5. Validation test of the Crank-Nicolson numerical scheme

A two-step process has been carried out for validating the implemented numerical procedure i. e. the *Crank-Nicolson method*. The primary step has been chosen to check the sensitivity of the mesh hence to ensure the accuracyof the scheme. In the secondary step, the numerical solutions are compared with simpler models from the scientific literature.

5.1. Sensitivity test

A proper grid-system is explored by conducting a '*mesh sensitivity test*' for the current investigation and it successfully offers an optimized and stable mesh. **Table 3**proposes an optimal grid-size (i.e., 100 X 500) with adequate accuracy (any additionalimprovement in the size of the mesh does not contribute to accuracy of the result). Similarly, '*time sensitivity test*' suggests an appropriate time-step size $\Delta t(t = h\Delta t, h = 0, 1, 2, \ldots) = 0.01$ as shownin **Table 4**.

5.2. Comparison with former special cases

A comparison study has been conductedto ensure accuracy of the numerical solutions for $\overline{C_f}$ and $\overline{Nu}$. The present investigation for heat transfer and fluid flow from a stationary cylinder $(\lambda = 0)$demonstrates very good correlation with earlier published results and hencegives the confirmation about the accuracy of the adopted numerical code i.e., Crank Nicolson type numerical scheme. At the primary stage of validation, impact of nano material (such as volume fraction, φ), viscous and elastic nature of third-grade $(\alpha_1, \alpha_2, \beta)$ are neglected in the absence of thermal radiation, magnetic field and supercritical conditions to examine only *Newtonian*characteristics of fluid flow (i.e., $\alpha_1 = \alpha_2 = \beta = \beta' = 0$) and matching the obtained results with early published results of Rani and Kim [63] $(\gamma = 0)$. **Figure 3**(comparative study) illustratesgraphical comparison of the implemented (Crank-Nicolson type) numerical finite difference scheme; clearly excellent corroboration is achieved and confidence in the Crank-Nicolson code is verified.

6. Graphical Results and Discussion

6.1. Accuracy of adopted RK-EOS model

Figures 4 and 5illustrate four curves for thermal expansion coefficient (β_T)versus temperature for supercritical water at two different pressures for experimental data [64], Redlich-Kwong-EOS [50], Van der Waals-EOS [52] and Ideal gas-EOS [65], respectively. However, for water, the coefficient of thermal expansion of perfect gas is evaluated as the inverse of the thermal field $(\mathrm{i.e}, \beta_T = 1/T)$. **Figures 4 and 5** clearly indicate that, the RK-EOS model provides an accurate depiction of the experimental database. Further, it is remarked that, the coefficient of thermal expansion deviates near the critical point. In general, at smaller pressures, the$\beta_T$of supercritical water (i.e., for liquids) enhances with temperature. On the other hand, for gases at smaller pressures, the coefficient of thermal expansion decays. Also, for *smaller temperatures*, a liquid like nature is noticed for high pressure isotherms whereas for *larger temperatures*, a gas like nature is observed. Further, for larger temperatures all isotherms tend to approach the ideal gas nature. Also, it is noticed that, when the working liquid is close to the critical point, the prediction of constant β_T fails and moreover β_T deviates at the exact critical point. Thus, the values calculated based on RK-EOS are more reasonable when compared to the VW-EOS and Ideal gas-EOS in supercritical region.

The critical values of the water such as P_c (critical pressure), V_c (critical volume), T_c (critical temperature), D_c (critical density),M' (critical mass), and Z_c (critical compressibility factor) are presented in**Table 5(a)**. The $\beta_T$values calculated based on RK-EOS using Table 5(a) are shown in **Tables 5(b) &5(c).**

The comparison of coefficient of thermal expansion values calculated based on RK-EOS [50] are compared with those values calculated based on empirical correlation [66], VW-EOS [52] and Ideal-gas equations [65] of state and are illustrated in **Fig. 6** at $T_r^* = 1.03$ amd $T_r^* = 1.58$. It is observed from **Fig. 6** that, the Nusselt number curve is plotted by employing RK-EOS (Ref. - Eqn. 28) lies very close to the experimental correlation curve. Thus, this comparison confirms the accuracy of the used RK-EOS model in the present study. Also, the results obtained based on RK-EOS are reliable in the SCF region.

$$\frac{Nu_X}{Ra_X^{1/4}} = \frac{4}{3}\left\{\frac{7\,Pr}{5(20+21Pr)}\right\}^{1/4} + \frac{4(272+315Pr)}{35(64+63Pr)}\left\{\frac{d}{l}Ra_X^{1/4}\right\}^{-1} \tag{28}$$

Table 1. Thermophysical propertiesof different nanoparticles ([53], [54], [58], [67] and [68]).

	$(\rho)_s$(kgq1`m^{-3})	$(k)_s$(Wm^{-1}k^{-1})	$(C_p)_s$(kg^{-1}k^{-1})	$(\beta_T)_s \times 10^{-5}$(k^{-1})
Ag	10,500	429	235	1.89

Table 2. Dynamic viscosity and thermal conductivity of different shapes of nanoparticles ([53] and [68]).

Model	Shape of nanoparticles	Dynamic viscosity	Thermal conductivity
(i)	Spherical	$\mu_{nf} = \frac{\mu_{bf}}{(1-\varphi)^{2.5}}$	$\frac{k_{nf}}{k_{bf}} = \frac{k_s + 2k_{bf} - 2\varphi(k_{bf} - k_s)}{k_s + 2k_{bf} + \varphi(k_{bf} - k_s)}$
(ii)	Spherical	$\mu_{nf} = \mu_{bf}(1 + 7.3\varphi + 123\varphi^2)$	$\frac{k_{nf}}{k_{bf}} = \frac{k_s + 2k_{bf} - 2\varphi(k_{bf} - k_s)}{k_s + 2k_{bf} + \varphi(k_{bf} - k_s)}$
(iii)	Cylindrical	$\mu_{nf} = \frac{\mu_{bf}}{(1-\varphi)^{2.5}}$	$\frac{k_{nf}}{k_{bf}} = \frac{2k_s + k_{bf} - 2\varphi(k_{bf} - k_s)}{2k_s + k_{bf} + 2\varphi(k_{bf} - k_s)}$
(iv)	Cylindrical	$\mu_{nf} = \mu_{bf}(1 + 7.3\varphi + 123\varphi^2)$	$\frac{k_{nf}}{k_{bf}} = \frac{2k_s + k_{bf} - 2\varphi(k_{bf} - k_s)}{2k_s + k_{bf} + 2\varphi(k_{bf} - k_s)}$

Table 3. Grid independency test at$P_r^* = 1.086$ and $T_r^* = 1.10$ in SCF region.

Grid size	Average Nusselt number $\alpha_1 = \alpha_2 = \beta' = 0.01, \beta = 0.6, \varphi = 0.04.$
25X125	0.1515531000
50X250	0.1538122000
100X500	0.1578322000
200X1000	0.1592252000

Table 4.Time-independency test at$P_r^* = 1.086$ and $T_r^* = 1.10$ in SCF region.

Time step size (Δt)	Average Nusselt number $\alpha_1 = \alpha_2 = \beta' = 0.01, \beta = 0.6, \varphi = 0.04$
0.1	0.1578331000
0.08	0.1578332000
0.05	0.1578330000
0.02	0.1578333000
0.01	0.1578322000

Table 5(a). Critical values of water [64] to calculate the fluid parameters for the present numerical simulations.

Compound chosen for study	P_c (MPa)	T_c (K)	V_c (cm^3/mol)	M' (kg/mol)	D_c (kg/m^3)	Z (-)
Water	22.090	647.30	55.95	0.01801528	322.0	0.229

Table 5(b). Thermal expansion coefficient in SCF region based on RK-EOS for different values of reduced pressure (P_r^*) with fixed $T_r^* = 1.011$.

P (MPa)	P_r^*	T' (K)	T_r^*	$(C_p)_{bf}$ (J/mol*K)	$(\mu)_{bf}$ (10^{-6} Pa*s)	$(k)_{bf}$ (W/m*K)	$(\rho)_{bf}$ (kg/m^3)	$(\beta_T)_{bf}$ (1/K)
44	1.99	655	1.011	118.65	70.944	0.47046	605.12	0.00382088
49	2.21	655	1.011	111.20	73.307	0.48352	622.09	0.00332480
54	2.44	655	1.011	105.86	75.383	0.49521	636.51	0.00296705
59	2.67	655	1.011	101.80	77.251	0.50591	649.13	0.00269430
64	2.89	655	1.011	98.567	78.961	0.51585	660.39	0.00247798

Table 5(c). Thermal expansion coefficient in SCF region based on RK-EOS for different values of reduced temperature (T_r^*) with fixed $P_r^* = 1.086$.

P	P_r^*	T'	T_r^*	$(C_p)_{bf}$	$(\mu)_{bf}$	$(k)_{bf}$	$(\rho)_{bf}$	$(\beta_T)_{bf}$

(MPa)		(K)		(J/mol*K)	(10^{-6} Pa*s)	(W/m*K)	(Kg/m^3)	(1/K)
24	1.086	684	1.05	144.59	27.927	0.12977	131.56	0.00832584
24	1.086	689	1.06	131.02	27.929	0.12398	125.91	0.00736239
24	1.086	694	1.07	120.48	27.976	0.11936	121.11	0.00663135
24	1.086	704	1.08	105.11	28.154	0.11252	113.27	0.00558684
24	1.086	714	1.10	94.377	28.407	0.10779	107.04	0.00486923

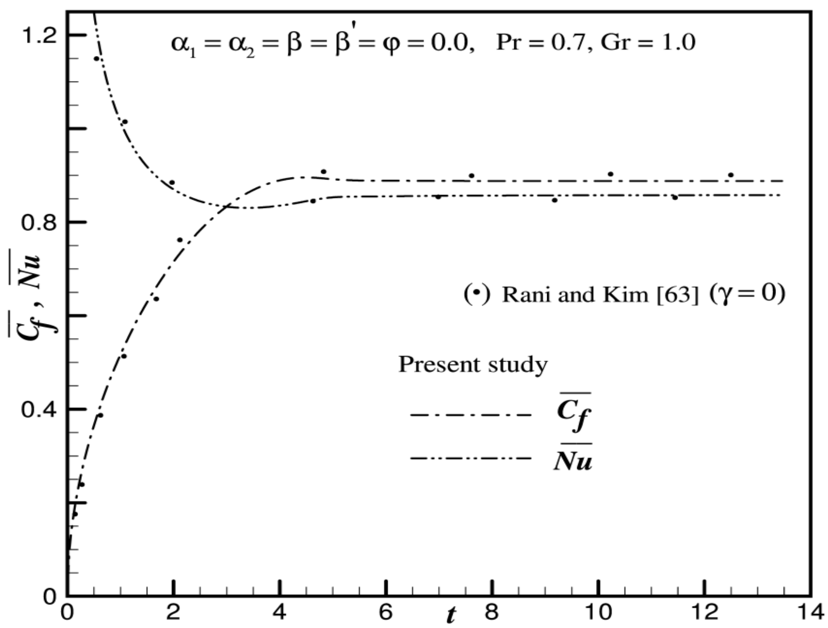

Fig. 3 Comparative study on Newtonian fluid.

Further validation with Rajesh et al. [69] is shown in Table 6 below and again excellent agreement with the present Crank-Nicolson numerical solutions is achieved.

Table 6: Transient velocity of various nanofluids whenPr = 6.2, Gr = 10, N = 3, φ = 0.04, X = 1.0, t = 0.2

	Numerical results of Rajesh et al. (2016) [69]		Numerical results of present study	
R	U	T	U	T
1.2	0.7891	0.4808	0.7080	0.4626

1.4	0.5088	0.1812	0.5001	0.1684
1.6	0.286	0.0548	0.214	0.0514
1.8	0.1444	0.0137	0.1248	0.0123
2.0	0.0665	0.0029	0.0565	0.0510

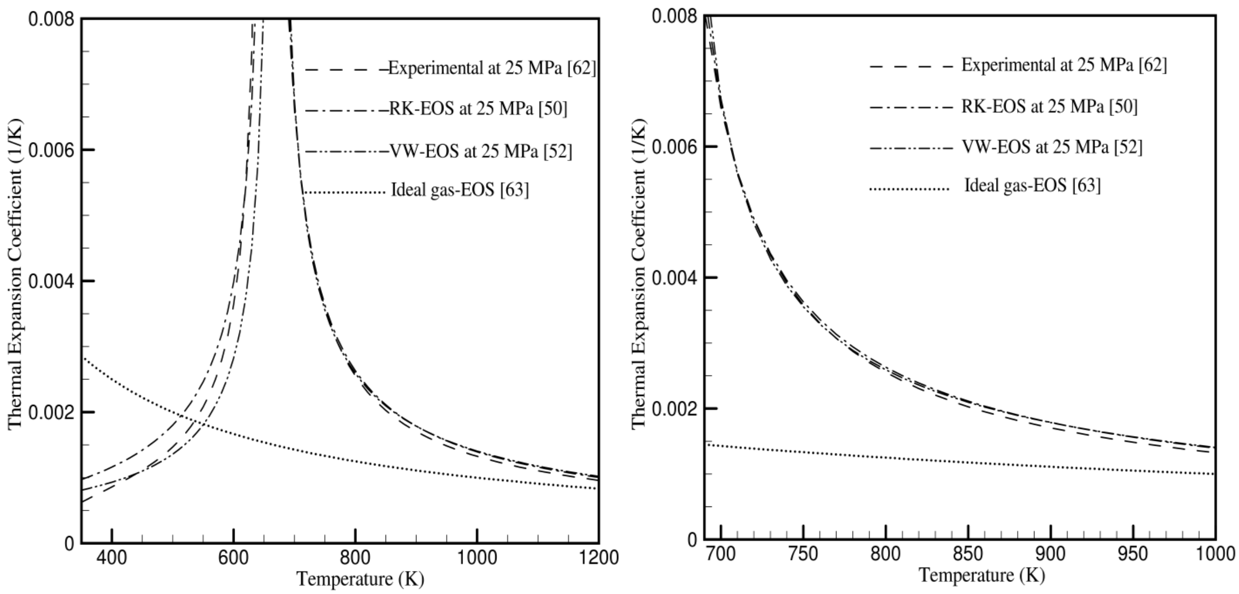

4 (a) **4 (b)**

Fig. 4(a) Comparison of volumetric coefficient of thermal expansion (β) of water based on VW-EOS [52], perfect-gas assumption [65] and RK-EOS [50] with experimental values [64] at 25 MPa and **(b)** an identical graph.

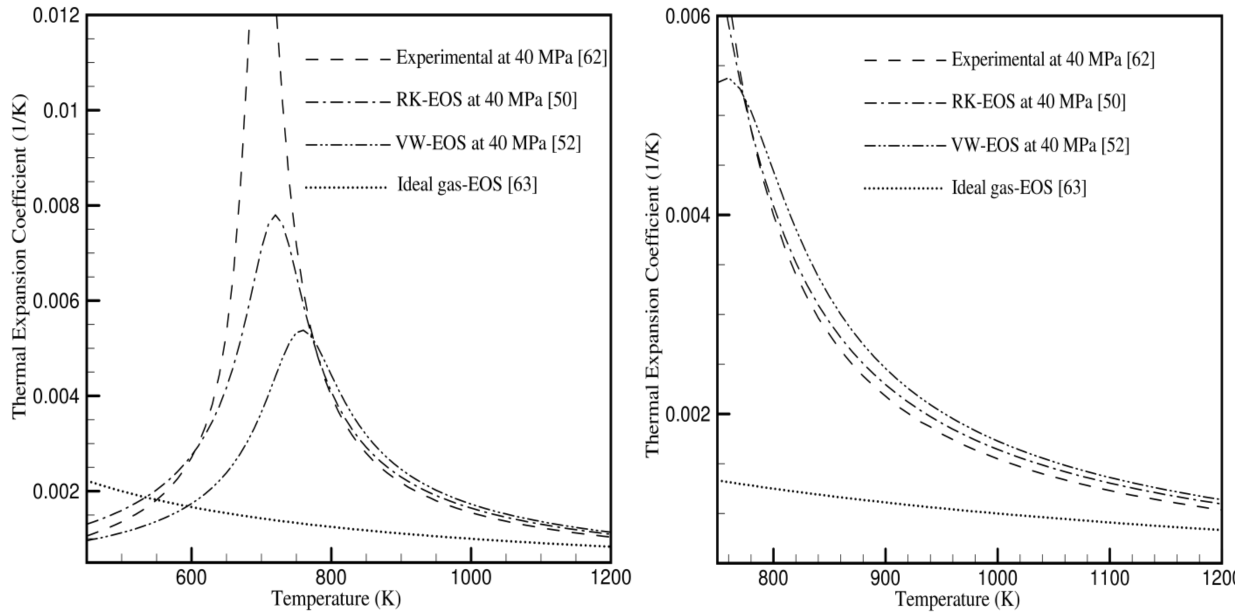

5(a) **5(b)**

Fig. 5(a) Comparison of volumetric coefficient of thermal expansion (β) of water based on VW-EOS [52], perfect-gas assumption [65] and RK-EOS [50] with experimental values [64] at 40 MPa and (**b**) an identical graph.

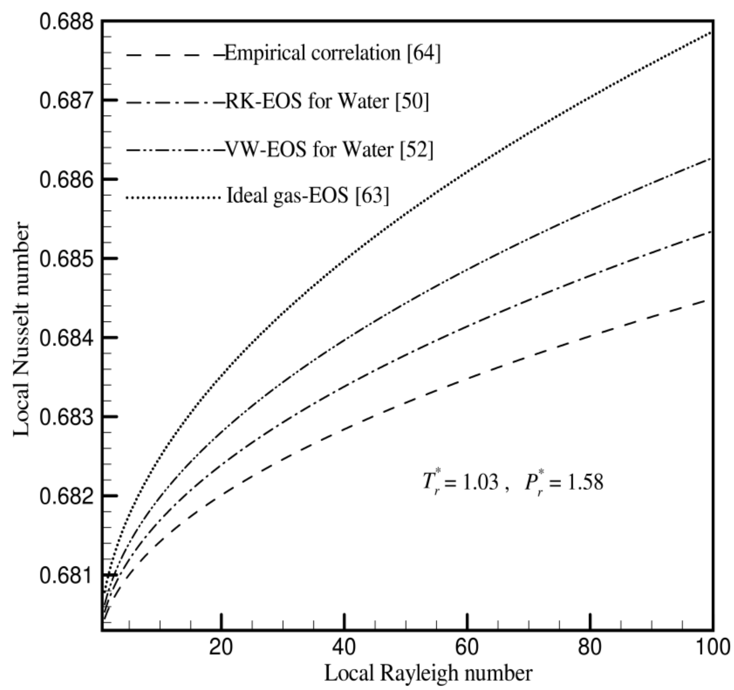

Fig. 6 Local Nusselt number (Nu_X) as a function of local Rayleigh number (Ra_X) for carbon di-oxide at $T_r^* = 1.03$ and $P_r^* = 1.58$ based on experimental correlation [66], RK-EOS [50], constant thermal expansion coefficient [65] and VW-EOS [52].

6.2. Flow variables

The variations in the flow fields (such as velocity and temperature) for supercritical thirdgrade nanofluidunder *unsteady and steady-state* conditions are investigated for the influential action of third-grade rheological parameter (β) and nanofluid volume fraction (φ). Also, the graphical results are drawn for variation in reduced pressure (P_r^*) and reduced temperature (T_r^*). Here, other parameters are kept constant such as$\alpha_1 = \alpha_2 = 0.01$ and modified third-grade parameter $\beta' = 0.01$, radiative parameter $N = 0.01$ and magnetic strength $M = 0.001$. Steady-state graphs of U &T for variation of β&φ over a moving cylinder($\lambda = 1$)and stationary cylinder($\lambda = 0$) are also depicted. With various values of reduced temperature, reduced pressure, third-grade parameter and volume fraction, numerically results for heattransfer rate (Nusselt number) and skin friction coefficient are also illustrated in graphs.The current investigation considers the *Ag*nanoparticles with viscoelastic third-grade fluid as base fluid.'$0 \leq \varphi \leq 0.04$' is the particular range for volume fraction of the silver nanoparticles, since they undergosedimentation after$\varphi > 8\%$. Here, spherically shaped nanoparticles with specific dynamic viscosity and thermal conductivity as referred from model **(i)** in **Table 2**are considered. Physical interpretation of the results is provided at length in the following discourse.

Relative results on supercritical third-grade nanofluid for stationary and moving cylinder

The numerically simulated comparative values of thermo-convective flow of thirdgrade nanofluid from stationary and moving cylinder under supercritical conditions are analyzed graphically. The considered geometry is circular cylinder in 2D flow-domain and subject to the boundary conditionsprescribed in Eqn. (11), $\lambda = 0$ or 1. Also, the subsequent paragraphs emphasize highlights in the hydrodynamic and heat transfer characteristics of thirdgrade nanofluid in both situations (i.e., $\lambda = 0$ &1) in SCF region.

(i) Transient results for stationary $(\lambda = 0)$**cylinder**

The time-dependent dimensionless velocity (U) profiles of thirdgrade nanofluid with *Ag*nanoparticles for differentP_r^*, T_r^*, β&φvalues at (1, 1.15) are illustrated in **Fig. 7 (a), 7(b) &7(c)**respectively. From all the figures in the SCF region, it is observed that the U curves retain a specific trend i.e., at an initial time (t<< 1) all curves are close enough to overlap each other (where conduction is the dominating factor); later,however, they deviate from each other (where convection is dominating) to reach the 'peak value'. With further elapse in time velocity profiles assume the *steady-state* position. A marked decrement in the magnitude of the overshoot of the velocity (U) curves is noted for higher values of T_r^*or P_r^*(refer **Figs. 7(a) & (b)**), the cause for this reduced overshoot is the '*velocity diffusion'* term, based on Eqn. (19). Therefore, greater resistance is offered to the supercritical thirdgrade nanofluid flow in the vicinity of the temporal maximum of$U$. From **Fig. 7(c)**, the U profile of thirdgrade nanofluid in SCF region at $\varphi = 0.02$showsa decreasing trend with magnifying values ofβ i.e., third-grade fluid with higher β has more viscous and lesser elastic nature which manifests in retardation in the boundary layer flow and a thicker hydrodynamic boundary layer thickness. Similarly, Ucurves of supercritical nanofluid at constant $\beta = 0.6$, are observed to be augmented with amplifying φ (volume fraction). Here, more nanoparticles are present for greaterφimplying greatercollision between the particles hence accelerating the fluid velocity and producing a thinner momentum boundary layer thickness. In both circumstances i.e., with intensifying φ or β values, the time for attaining steady statevalues is almost the same. It is clearly observed that with variation in β, the gap between the curve is more pronounced than for variation in φ.

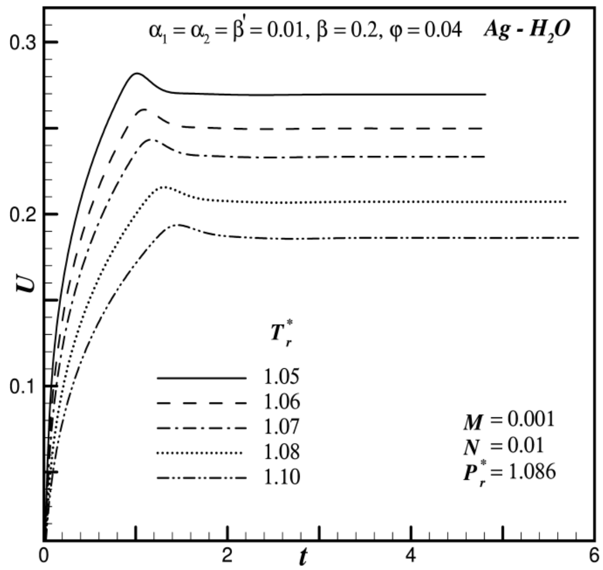

7(a)

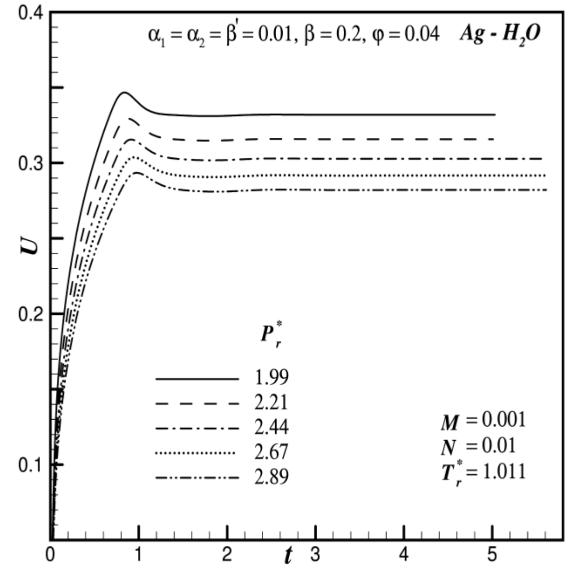

7(b)

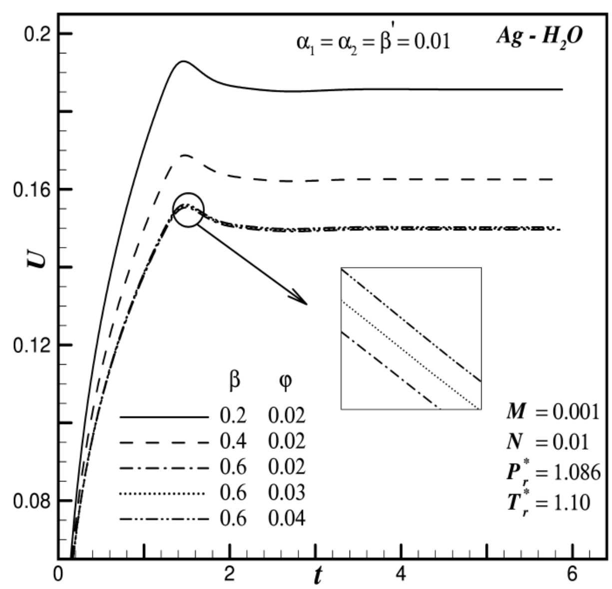

7(c)

Fig. 7 Transient velocity profile at different **(a)** reduced temperature; **(b)** reduced pressure; **(c)**third-grade fluid parameter and volume fraction for $\lambda = 0$.

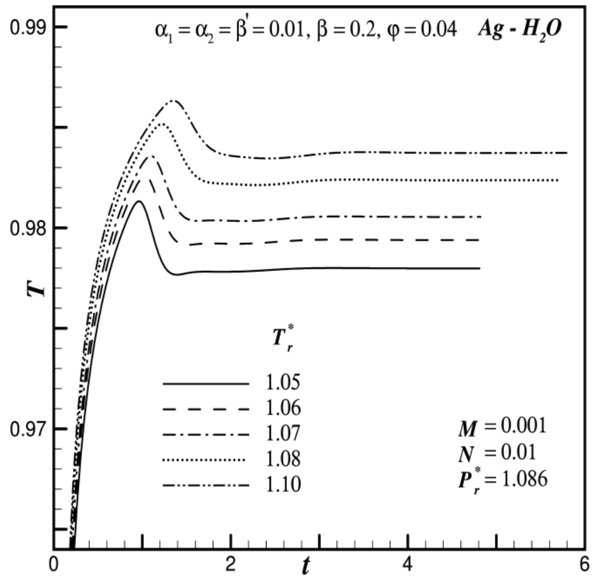

8(a)

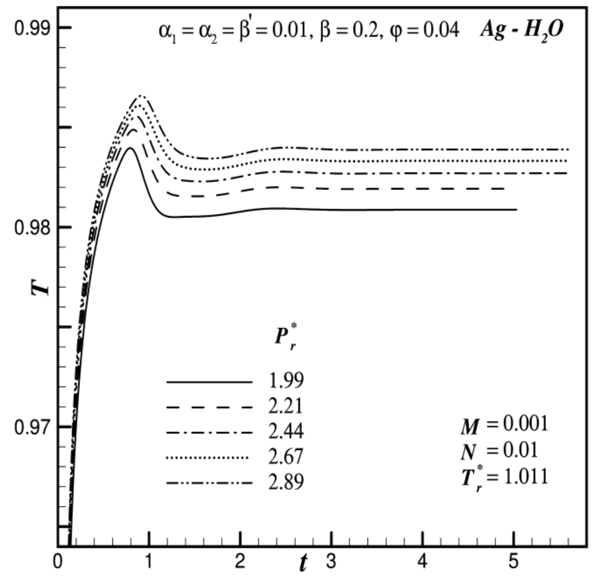

8(b)

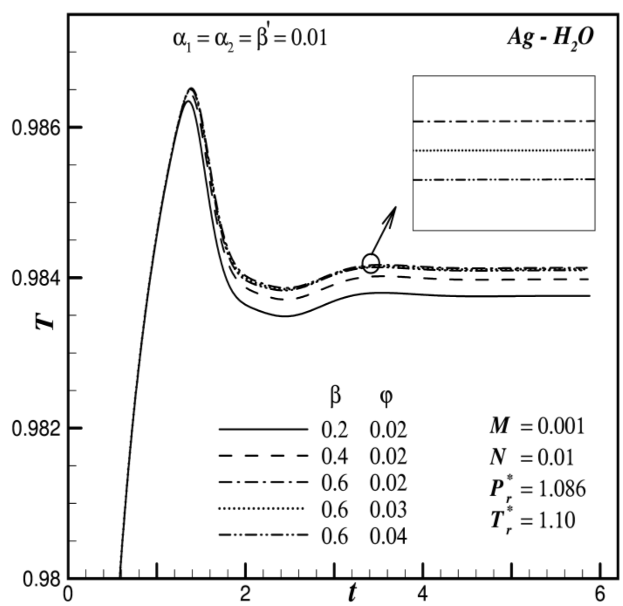

8(c)

Fig. 8 Transient temperature profile at different **(a)** reduced temperature; **(b)** reduced pressure; **(c)** third-grade fluid parameter and volume fraction for $\lambda = 0$.

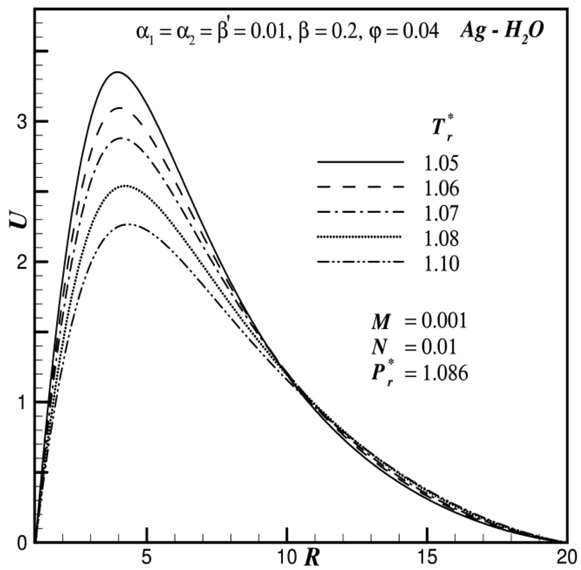

9(a)

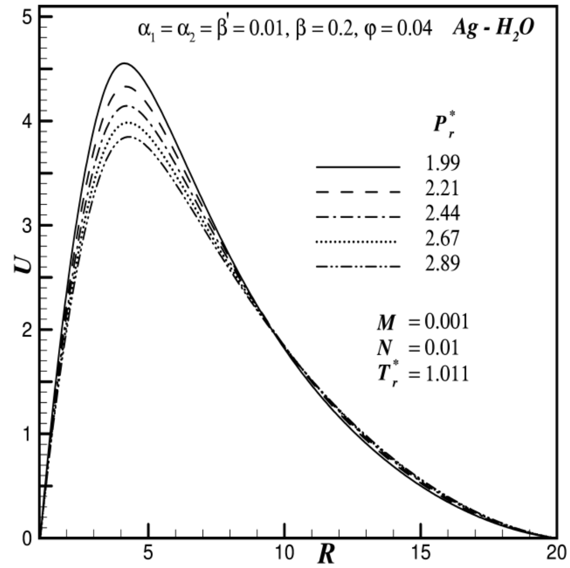

9(b)

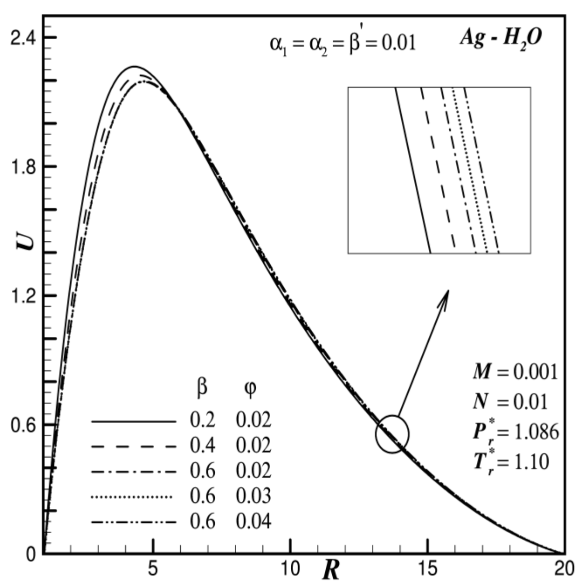

9(c)

Fig. 9 Time-independent velocity profile at different **(a)** reduced temperature; **(b)** reduced pressure; **(c)** third-grade fluid parameter and volume fraction for $\lambda = 0$.

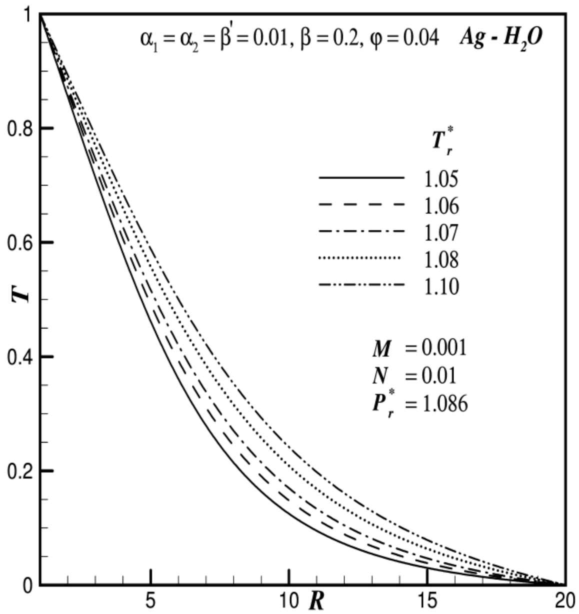

10(a)

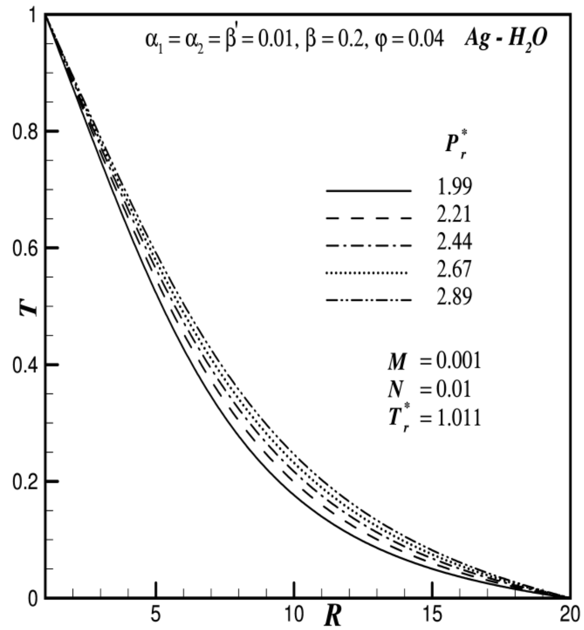

10(b)

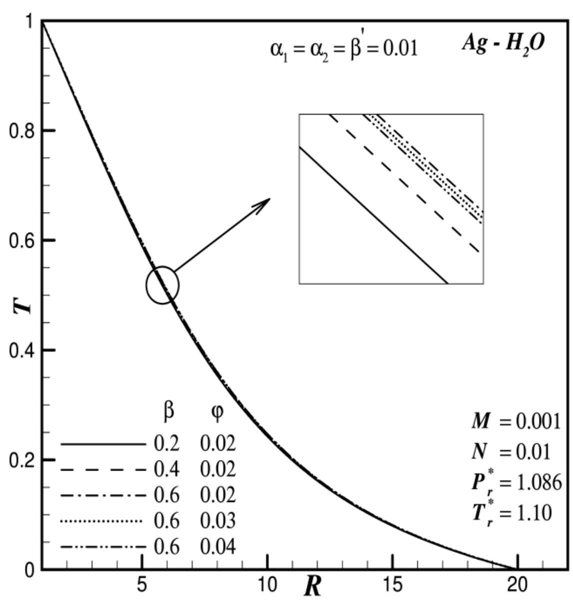

10(c)

Fig. 10 Time-independent temperature profile at different **(a)** reduced temperature; **(b)** reduced pressure; **(c)** third-grade fluid parameter & volume fraction for $\lambda = 0$.

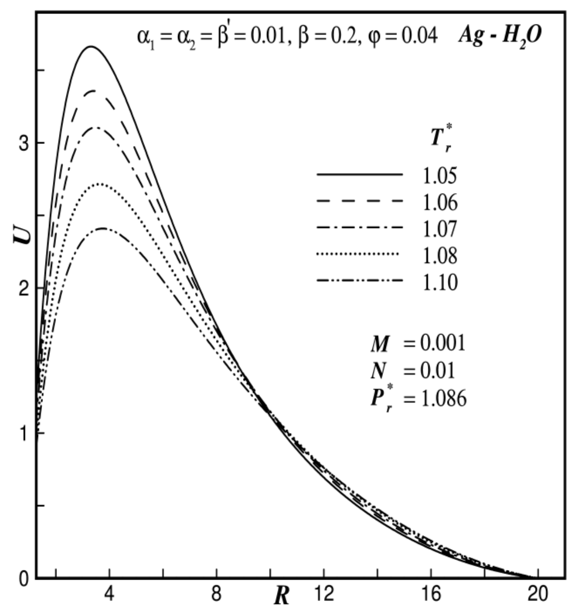

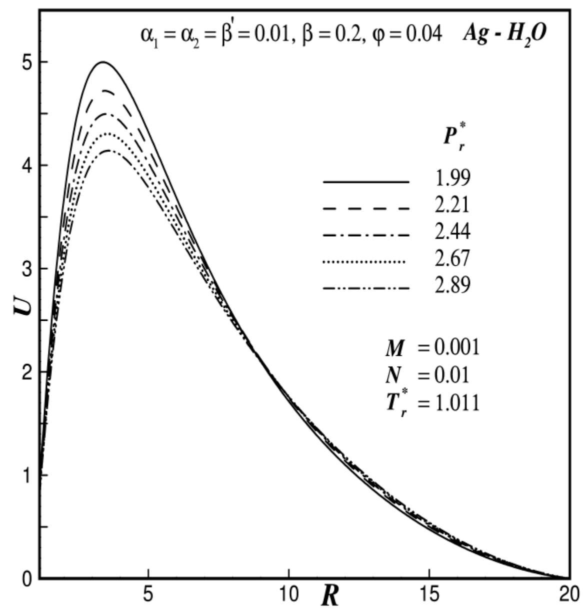

11(a) **11(b)**

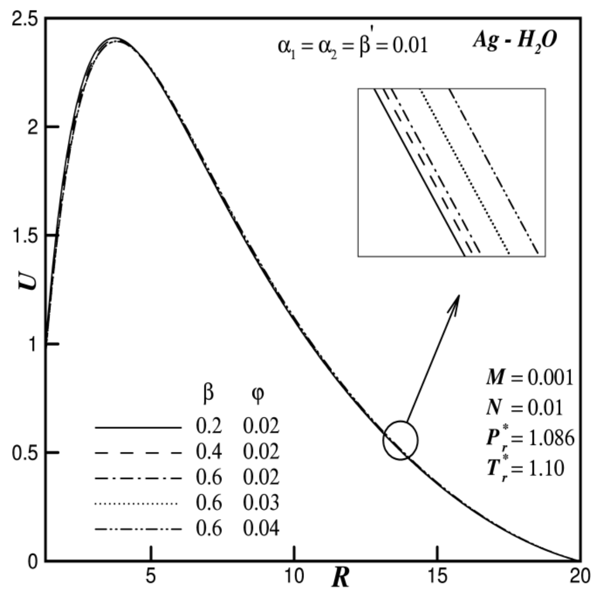

11(c)

Fig. 11 Time-independent velocity profile from moving cylinder at different **(a)** reduced temperature; **(b)** reduced pressure; **(c)** third-grade fluid parameter & volume fraction for $\lambda = 1$.

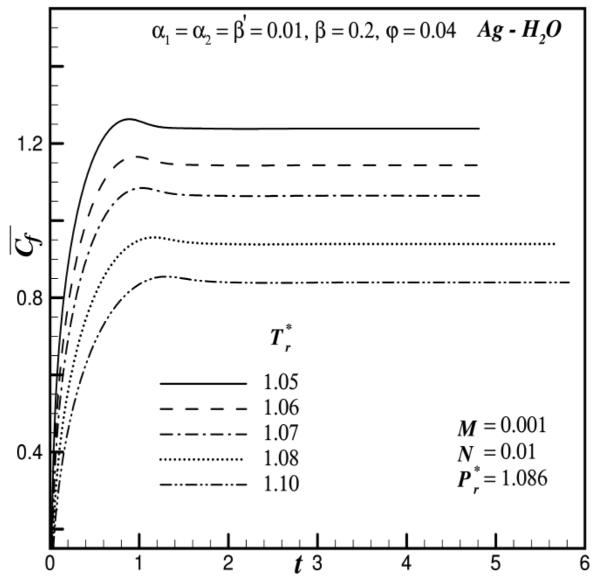

12(a)

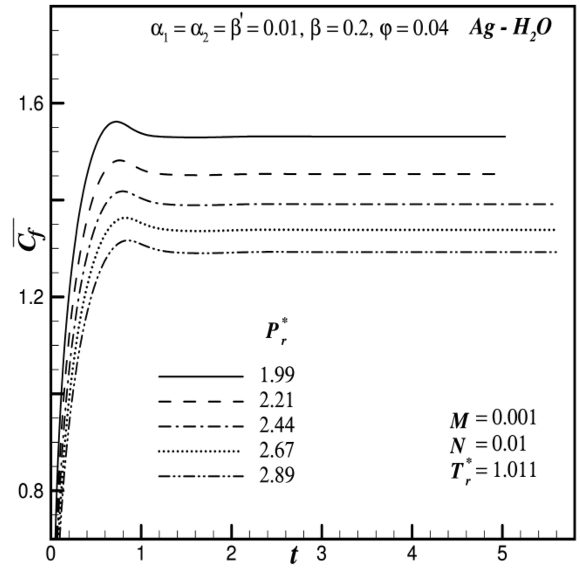

12(b)

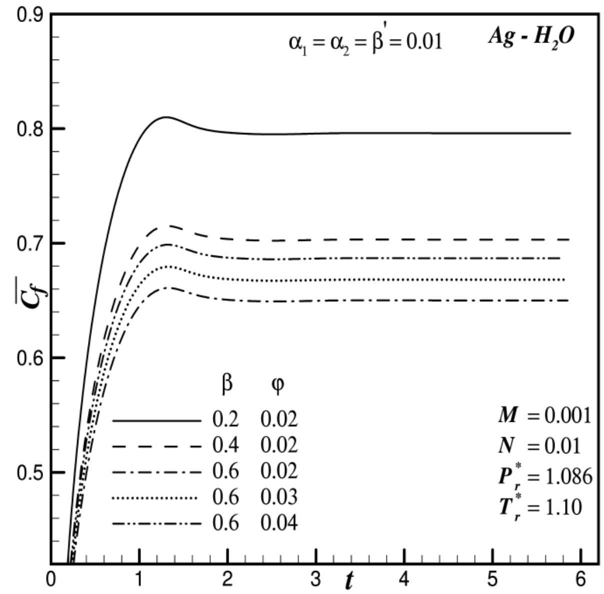

12(c)

Fig. 12 Coefficient of average skin friction at different **(a)** reduced temperature; **(b)** reduced pressure; **(c)** third-grade fluid parameter and volume fraction for $\lambda = 0$.

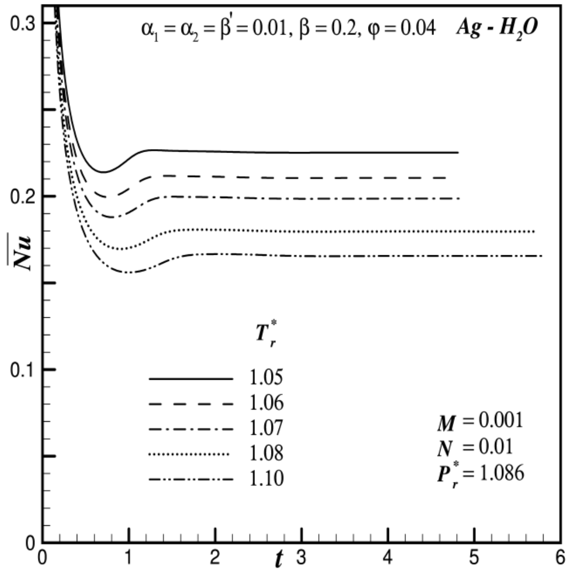

13(a)

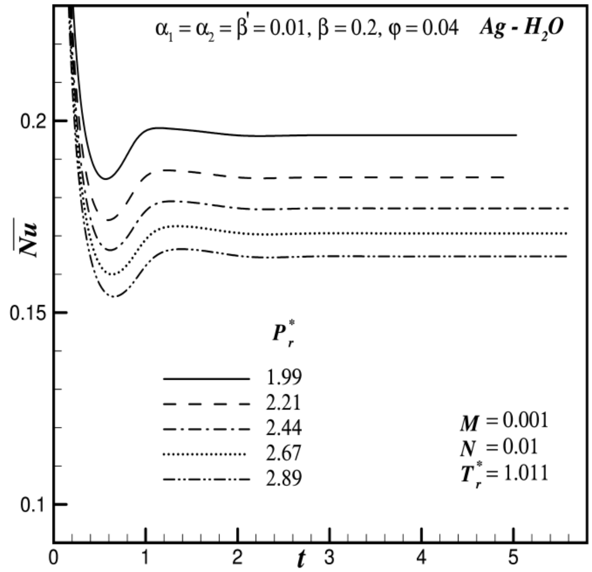

13(b)

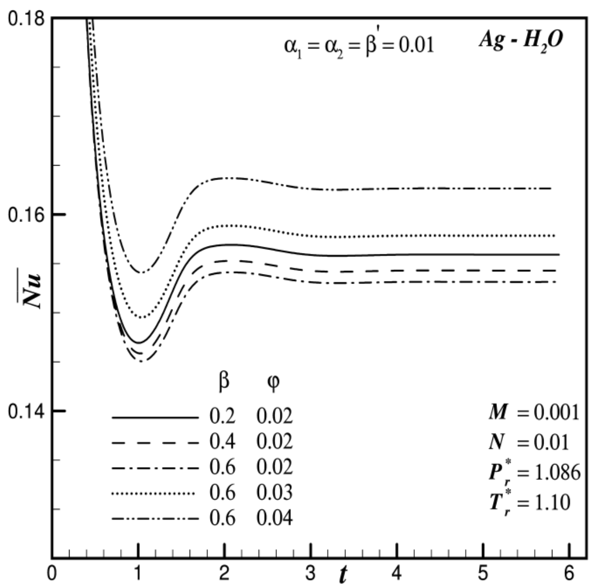

13(c)

Fig. 13 Coefficient of average heat transfer at different **(a)** reduced temperature; **(b)** reduced pressure; **(c)** third-grade fluid parameter & volume fraction for $\lambda = 0$.

Unsteady temperatureprofiles(T) forthirdgrade nanofluid withvariation ofT_r^*, P_r^*,βandφ, at (*X=1, R=1.15*) are depicted in **Figs. 8(a), (b) & (c)**. As the flow starts (t<< 1), the T curves (observed from all figures) overlap one another (i.e., *conduction*is the dominant heat transfer mode). Thereafter they diverge from each other (i.e., *free convection*is the dominant heat transfer mode)achieveT_{max} (temporal maximum value) and subsequently attain the *time-independent state*. At any specific location of the boundary layer flow region, transient behavior exhibited by all the$T$ curves is similar. These observations are also remarkably similar for variations in all parameters such as T_r^*, P_r^*, β and φ (refer to**Figs. 8(a), (b) & (c)**). **Figures 8(a) & (b)**, indicate that the magnitude of the temperature isenhanced distinctly by varying T_r^*&P_r^* at constant φ&β. This temperature variation in the supercritical region of nanofluid is expected since enhancing T_r^*or P_r^*leads to a reduction in Gr (Grashof number) and increment in Pr (Prandtl number), which intern augments the temperature.

For that reason, it is noteworthy to remark that Gr takes a prominent role when compared to Prin supercritical thirdgrade nanofluid flow. From **Fig. 8(c)**, it is observed that as β increases, temperature is enhanced. The reason behind this observation is that higher $\beta$the viscous nature of the fluid which improves thermal diffusion and results in a thicker thermal boundary layer. A contrary result is witnessed for the variation in φ (refer **Fig. 8(c)**). Greater φ value adds morenanoparticles to the flow-field hence there will be more heat transfer. The gap between the T curves withβ variation is highas compared to variation in φ indicating a greater sensitivity of the temperature field to viscoelasticity rather than Nanoscale effects. The time required to reach the peak value increases with augmentation in any of the parameters (i.e., β, φ, T_r^* and P_r^*).

(ii)Steady-state results for stationary $(\lambda = 0)$**cylinder**

The steadystate$U$ −profiles for thirdgrade nanofluid with variations in T_r^*,P_r^*, β and φagainst radial coordinate at $X = 1.0$are depicted in **Figs. 9(a), (b) & (c)**. The velocity curves of the nanofluid followa consistent trend for the variation in parameters (T_r^*,P_r^*, φ and β). In all cases (i.e., increasing β or φ or T_r^* orP_r^*), velocity of the fluid is elevated to the maximum (U_{max}) value and thereafter decays gradually to zero velocity (i.e., $U = 0$). Magnitude of U_{max} decreases with increasing β or T_r^* orP_r^*, whereas with augmenting φ, it is almost constant. By varying any of the parameters, the steady-state velocity curves change with increasing trend after a certain radial coordinate,R. It is evident that the variation in the fluid velocity is more pronouncedwith different T_r^* values, as compared to P_r^* variation. As T_r^* or P_r^* enhances, the velocity diffusion intensifies. Hence, a modification in velocity magnitudes arises. For increased P_r^* and T_r^*, the convection currents are intensified very close to a hot cylindrical surface, however this effect is stifled further away from the hot surface. Consequently, the larger$U$magnitudes are witnessed adjacent to the hot wall.

Likewise, the steady-state plots are drawn for temperature variations by varying different parameters (i.e., T_r^*,P_r^*,β and φ)in **Figs. 10(a), (b) & (c)**, respectively). Here also, all T profiles for different T_r^* orP_r^*or β or φfollows the same path i.e., initially attaining the highest value $T = 1$(i.e., *boundary condition maintained at hotter surface of the cylinder*) and as we move away from the cylinder T curves are suppressed to the lowest value (i.e., $T = 0$ in the free stream). Also, heat transfer by the conductive mode is dominated at the starting time. Impact of T_r^* orP_r^*variations on temperature of flow regime is more effective than β or φ. A significant observation from these figuresis that the thickness of thermal boundary layer increases for intensifying β or T_r^* orP_r^*; however, the reverse trend is observed with respect by augmenting φ. From **Figs. 10(a) & (b)**, effect of T_r^* is significantly more impactful relative to that of P_r^*.

(iii) Steady-state results for moving $(\lambda = 1)$**cylinder**

Figures 11(a), (b) & (c)visualize the numerically results forsteady-state U (non-dimensional velocity) values of the thirdgrade nanofluid for moving $(\lambda = 1)$cylinder (with velocity $u_0$along the radial direction) in the SCF region with varying values of T_r^*,P_r^*, β and φ, respectively. Here, elevation in velocity of the viscoelastic nanofluid is observed. All the results on velocity of the fluid flow with varying different parameters are similar with results related to the case of stationary cylinder as witnessed from **Figs. 7(a), (b) & (c)**. The key observations which can be made are; (i) the velocity curves initiate with $U = 1$and attain the U_{max}(peak steady-state velocity) then fall to $U = 0$ (the minimum value), (ii) the magnitude of the attained velocity at all cases (i.e., at different parameter variations) is greater compared to those computed at stationary cylinder.

7. Results on coefficients of heat transfer and skin friction

To satisfy the design criteria in material processing, cooling/heating techniques, energy and waste management, there is a crucial demand for the calculation ofheat transfer rate $\overline{Nu}$and skin friction coefficient$\overline{C_f}$. In the current problem, non-Newtonian supercritical thirdgrade nanofluid, the Nusselt number and skin friction coefficient will therefore also provide very useful insights into the wall gradient conditions. The dimensionless equations to calculate $\overline{C_f}$ and $\overline{Nu}$ are specified through following equations.

$$\overline{C_f} = \frac{B}{Re}\int_0^1 \left(\frac{\partial U}{\partial R}\right)_{R=1} dX \tag{29}$$

$$\overline{Nu} = -E\int_0^1 \left(\frac{\partial T}{\partial R}\right)_{R=1} dX \tag{30}$$

where$Re = \frac{u_0 r_0}{v_f}$is the local Reynolds number.

The rate of variation in the skin friction coefficient with reduced temperature(T_r^*), reduced pressure (P_r^*), supercritical thirdgrade nanofluid parameter (β) and the volume fraction (φ)at $\lambda = 0$are illustrated in **Figs.12(a), (b) & (c)**, respectively. All skin friction coefficient ($\overline{C_f}$) profiles show increasing an trend tothe peak value, drops to smaller value then as time elapses attain the constant value. Higher skin friction values are observed with increment in P_r^* and lower $\overline{C_f}$values are induced by elevating φ i.e., volume fraction of the nanoparticles. Also, from **Fig. 12(c),** it is evident that skin friction (dimensionless surface shear stress) are more sensitive to β variation than φ, i.e., the gap between the $\overline{C_f}$ curves is more for β variation. With increment in β, $\overline{C_f}$magnitudes descend i.e., decelerated thirdgrade nanofluid flow is induced (thicker momentum boundary layer) which are verified through **Fig. 7(c)**.This is attributable to βaugmenting the viscoelastic nature of the thirdgrade nanofluid. **Figure 12(c)** also displays resultswith varying φ i.e., for higherφ (greater percentage doping of nanoparticles), the skin friction ($\overline{C_f}$) exhibited by the fluid is enhanced (**Figure7(c)**supports this result) and this is attributable to the enhanced ballistic collisions associated with greater concentrations of nanoparticles.

The heat transfer characteristics at $R = 1$ of the hot surface of stationary cylinder ($\lambda = 0$) for supercritical thirdgrade nanofluid flow with variations in T_r^*,P_r^*, φ and β are shown through **Figs. 13(a), (b) & (c),** respectively. At early times, $\overline{Nu}$ curvesare strongly reduced to lower values, and this behaviour intensifieswhen the time-independent state (i.e., constant value) occurs. At the initial stages of the flow, $\overline{Nu}$curves are overlapped with each other due to the thermal conduction effect on heat transfer rates. It is witnessed from the **Figs. 13(a)** and **13(b)** that a contrary relation can be observed for $\overline{Nu}$ values pertaining to P_r^* and T_r^* variations. This observation is associated with the fact that in the SCF region of the third grade nanofluid, the temperature values enhance for augmenting P_r^* or T_r^*; hence a decrement is noticed in $\overline{Nu}$. (Refer to Eqn. (30) and **Fig. 8**). With increasing β (supercritical thirdgrade nanofluid parameter), ($\overline{Nu}$) diminishes. The effect of β on heat transfer of third-grade fluid is therefore to inhibit heat transferred to the cylinder surface which concurs with the trends in **Fig. 13(c)**. Higher β value implies formation of stronger bonds between the fluid particles (greater elastic forces) which results in an elevation in thermal conduction effect and therefore temperature of the supercritical nanofluid regime (refer **Fig. 8(c))**. Therefore, the thermal boundary layer of supercritical nanofluid flow is increased and a slower rate of heat transfer to the hot cylinder. Also, for enhanced φ (volume fraction) value, $\overline{Nu}$ takes greater values due to the increased number of nanoparticles in the nanofluid, of supercritical nanofluid there will be more rate of heat transfer (refer **Figs. 8(c)**& **13(c)**).

8. Concluding remarks

A numerical investigation has been conducted to study the transient magnetohydrodynamic free convective flow of supercritical thirdgrade nanofluid from a vertical moving/stationary hot cylinder with thermal radiation. The influential actions of third-grade fluid parameter, reduced pressure,reduced temperature and volume fraction of nanoparticles in the presence of constant magnetic and thermal radiation effect are studied in supercritical region.A numerical implicit finite difference scheme (*Crank-Nicolson type*)has been deployed to solve the transformed, dimensionless coupled nonlinear momentum and energy boundary layer equations. Mesh independence and benchmarking with previous studies are included. Thethermofluid characteristics are scrutinized by varying different parameters. The major findings of the present numerical study may be listed as follows:

- RK-EOS model based thermodynamic model has been introduced to more accurately analyze the convective flow behaviors of supercritical thirdgrade nanofluid.

- The values of β_T as calculated for the water based nanofluid on RK-EOS are closerto the experimental values than those based on the ideal gas assumption and VW-EOS.
- For thirdgrade nanofluid under supercritical conditions, unsteady velocities increase, and temperature values decrease, as volume fraction of the nanofluid is elevated. Correspondingly, with higher values of third-grade fluid parameter, velocity decreases and temperature is enhanced at transient times.
- A relative increase in heat transfer of the nanofluid flow is observed from the case of the moving cylinder to that of the stationary cylinder.
- Heat transfer characteristics of non-Newtonian supercritical nanofluid are enhanced with lower third-grade fluid parameter and increased volume fraction. Also, skin friction values are boosted with a decrement in third-grade fluid parameter value and increment in nanoparticle volume fraction.
- For higher values of reduced temperature and reduced pressure, lower velocity values are noticed. But the reverse observation can be found with respect to temperature.
- Lower heat transfer and skin friction characteristics are observed at increasing values of reduced temperature and reduced pressure.

The present study has provided some useful insights into external supercritical magnetic nanofluid boundary layer flows. Also, the considered numerical technique (‘*Crank-Nicolson scheme’*) has been shown to be an efficient, accurate methodology for simulating viscoelastic characteristics. However viscous dissipation, Newtonian heating, and hydrodynamic slip conditions have been neglected. Furthermore, there are alternative rheological models e. g. micropolar, polar (couple stress) and viscoplastic models which may be explored. Efforts in these directions are currently ongoing and will be communicated immediately.

Acknowledgements

The authors appreciate greatly the comments of the reviewers which have served to improve the present work.

References

1. Q. Liu, X. Ding, B. Du and T. Fang, Multi-phase equilibrium and solubilities of aromatic compounds and inorganic compounds in sub and supercritical water: a review.*Crit. Rev. Anal. Chem*. 0, 1–11, (2017).

2. G. Caputo, P. Rubio, F. Scargiali, G. Marotta and A. Brucato,Experimental and fluid dynamic study of continuoussupercritical water gasification of glucose,*J. Supercrit.Fluids*107, 450–451, (2016).

3. S. Toyama, H. Hayashi, M. Takesue, M. Watanabe and R. L. Smith, Synthesis of alkali niobate $K_{1-x}Na_xNbO_3$nanoparticles using supercritical water flow system,*J.Supercrit. Fluids*107, 1–8, (2016).

4. T. Zhang and D. Che, Numerical investigation on heattransfer of supercritical water in a roughened tube,*Numer.Heat Transf*. A 69, 558–573, (2016).

5. L. Zhang, B. Caia, Y. Wenga, H. Gua, H. Wanga, H. Li andV. Chatoorgoon, Experimental investigations on flowcharacteristics of two parallel channels in a forced circulation loop with supercritical water,*Appl. Therm. Eng*.,106,98–108, (2016).

6. Z. Q. Long and P. Zhang, Natural convection heat transferof supercritical helium in a closed vertical cylinder,*Cryogenics*,61, 120–126, (2014).

7. P. Forooghi and K. Hooman, Experimental analysis ofheat transfer of supercritical fluids in plate heat exchangers,*Int. J. Heat Mass Transf*., 74, 48–459, (2014).
8. Z. Q. Long, P. Zhang, B. Shen and T. Li, Experimentalinvestigation of natural convection in a supercritical binaryfluid,*Int. J. Heat Mass Transf*.,90, 922–930, (2015).
9. X. Lei, H. Li, Y. Zhang and W. Zhang, Effect of buoyancyon the mechanism of heat transfer deterioration of supercritical water in horizontal tubes,*ASME J. Heat Transf*.,135,071703–9, (2013).
10. P. E. Savage, Heterogeneous catalysis in supercriticalwater,*Catal. Today*,62, 167–173, (2000).
11. Y. Lu, T. Zhang and X. Dong, Numerical analysis of heattransfer and solid volume fraction profiles around a horizontal tube immersed in a supercritical water fluidized bed.*Appl. Therm. Eng*.,93, 200–213, (2016).
12. Y. Arai, T. Sako and Y. Takebayashi, Supercritical Fluids, Springer, Berlin (2002).
13. C. Domingo and P. S. Peternault, *Supercritical Fluid Nanotechnology: Advances and Applications in Composites and Hybrid Nanomaterial's*. Pan Stanford Publishing CRC press Taylor and Francis Group, Boca Raton, USA (2016).
14. G. Brunner,*Topics in Physical Chemistry*: *Gas Extraction*. Springer, Berlin (1994).
15. J. Hui, Z. Xiao, X. Su, C. Zhu, C. Cao and L. Guo, Supercritical water synthesis of bimetallic catalyst and its application in hydrogen production by furfural gasification in supercritical water,*Int. J. Hydrog. Energy*, 42, 4943– 4950, (2017).

16. D. Guzonas, M. Edwards, and W. Zheng, Assessment of candidate fuel cladding alloys for the Canadian supercritical water-cooled reactor concept,*J. Nuclear Eng. Rad. Sci*.,2, 011016–8, (2016).

17. T. Schulenberg, K. H. L. Laurence and Y. Oka, Review of R&D for supercritical water cooled reactors,*Prog. Nuclear Energy*,77, 282–299, (2014).

18. E. Kiran, P. G. Debenedetti and C. J. Peters, *Supercritical Fluids: Fundamentals and Applications*, NATO Science Series, Netherlands: Springer (2000).

19. M. Hosseinpour, S. Fatemi and S. Javad, Deuterium tracing study of unsaturated aliphatics hydrogenation by supercritical water during upgrading of petroleum heavy oil. Part I: Noncatalytic cracking,*J. Supercrit. Fluids*,107, 278–285, (2016).

20. V. R. Maitri, C. Zhang and J. Jiang, Computational fluid dynamic assisted control system design methodology using system identification technique for CANDU supercritical water cooled reactor (SCWR),*Appl. Therm. Eng*.,118, 17–22, (2017).

21. M. Gaudet, M. Yetisir and A. Sartipi, Conceptual plant layout of the Canadian generation IV supercritical water-cooled reactor,*CNL Nuclear Rev*.,5, 203–219 (2016).

22. A. Kiss, M. Balasko, L. Horvath, Z. Kis and A. Aszodi, Experimental investigation of the thermal hydraulics of supercritical water under natural circulation in a closed loop,*Ann. Nucl. Energy*,100, 178–203, (2017).

23. Y. M. Alshammari and K. Hellgardt, Sub and supercritical water reforming of n hexadecane in a tubular flow reactor,*J. Supercrit. Fluids*,107, 723–732, (2016).

24. S. U. S. Choi,Enhancing thermal conductivity of fluids with nanoparticles. In: Siginer, D.A., Wang, H.P. (eds.) *Developments and Applications of Non-Newtonian flows*, American Society of Mechanical Engineers, New York (1995).

25. H. Masuda, A. Ebata, K. Teramae andN. Hishinuma, Alteration of thermal conductivity and viscosity of liquid by dispersing ultra-fine particles (dispersion and Al_2O_3, SiO_2, and Tio_2ultra-fine particles), *NetsuBussei (Japan)*,7(4), 227-33 (1993).

26. J. A. Eastman, S. U. S Choi, S. Li, L. J. Thompson andS. Lee, Enhanced thermal conductivity through the development of nanofluids,*Mater. Res. Soci. Symp. Proceedings*, Pittsburgh, PA, 457, 3-11, (1997).

27. K.S. Gandhi, Thermal properties of nanofluids:controversy in making,*Current Science*, 92(6), 717-18, (2007).

28. D. Yulong, H. Alias, D. Wen andR. A. Williams, Heat transfer of aqueous suspensions of carbon nanotubes (CNT nanofluids), *Int. J. Heat & Mass Transfer*, 49, 240-50, (2006).

29. T. Thumma, O. Anwar Bég and A. Kadir, Numerical study of heat source/sink effects on dissipative magnetic nanofluid flow from a non-linear inclined stretching/shrinking sheet, *J. Molecular Liquids*, 232, 159-173 (2017).

30. O. Anwar Bég, S. Kuharat, M. Ferdows, M. Das, A. Kadir, M. Shamshuddin, Magnetic nano-polymer flow with magnetic induction and nanoparticle solid volume fraction effects: *solar magnetic nano-polymer fabrication simulation, Proc. IMechE-Part N: J Nanoengineering, Nanomaterials and Nano-systems (2019).* DOI: 10.1177/ 2397791419838714 (19 pages).

31. Hayat, F.M. Abbasi, M. Al-Yami, and S. Monaquel, Slip and Joule heating effects in mixed convection peristaltic transport of nanofluid with Soret and Dufour effects, *Journal of Molecular Liquids* 194, 93-99 (2014).

32. J. Prakash, E.P. Siva, D Tripathi, S. Kuharat and O. Anwar Bég, Peristaltic pumping of magnetic nanofluids with thermal radiation and temperature-dependent viscosity effects: modelling a solar magneto-biomimetic nanopump, *Renewable Energy*(2018). 18 pages.

33. Wenjea J. Tseng, Chun-Nan Chen, Effect of polymeric dispersant on rheological behavior of nickel/terpineol suspensions, *Materials Science and Engineering* A347 145/153 (2003).

34. Kathy lu, Rheological behavior of carbon nanotube-alumina nanoparticle dispersion systems, Powder Technology, 177 (3), 154-161, (2007).

35. Tran X. Phuoc, Mehrdad Massoudi, Experimental observations of the effects of shear rates and particle concentration on the viscosity of Fe_2O_3–deionized water nanofluids, *International Journal of Thermal Sciences*, 48,1294-1301, (2009).

36. Haisheng Chen, Yulong Ding, Alexei Lapkin, Rheological behaviour of nanofluids containing tube / rod-like nanoparticles, *Powder Technology*, 194, 132–141, (2009).

37. T. Javed and I. Mustafa, Slip effects on a mixed convection flow of a third-grade fluid near the orthogonal stagnation point on a vertical surface, *J. Applied Mechanics and Technical Physics*, 57, 527–536 (2016).

38. O. Anwar Bég, H. S. Takhar, R. Bhargava, S. Rawatand V. R. Prasad, Numerical study of heat transfer of a third-grade viscoelastic fluid in a non-Darcy porous media with thermophysical effects, *Physica Scripta*, 77, 065402-13, (2008).

39. G. J. Reddy, A. Hiremath, and M. Kumar, Computational modeling of unsteady third-grade fluid flow over a vertical cylinder: a study of heat transfer visualization, *Results in Physics*, 8, 671-682, (2018).

40. G. J. Reddy, A. Hiremath, Hussain Basha and N. S. Venkata Narayanan, Transient flow and heat transfer characteristics of non-Newtonian supercritical third-grade fluid (CO_2) past a vertical cylinder, *International Journal of Chemical Reactor Engineering*, 20170232 (2018).

41. A. Hiremath, G. J. Reddy, M. Kumar and O. Anwar B´eg, Unsteady free convective heat transfer in third-grade fluid flow from an isothermal vertical plate: A thermodynamic analysis, *International Journal of Modern Physics B* 33, (08) 1950060 (2019).

42. A. Hiremath and G. J. Reddy, Transient analysis of third-grade fluid flow past a vertical cylinder embedded in a porous medium, *Numerical Heat Transfer and Fluid Flow, Lecture Notes in Mechanical Engineering*, 83-91 (2019).

43. A. Hiremath, G. J. Reddy and O. Anwar Bég, Computational unsteady flow analysis for third-grade fluid from an isothermal vertical cylinder through a Darcian porous medium, *Heat Transfer-Asian Research*, 48 (7), 2752-2772 (2019).

44. A. Hiremath, G. J. Reddy and O. Anwar Bég, Transient analysis of third-grade viscoelastic nanofluid flow external to a heatedcylinder with buoyancy effects, *Arabian Journal for Science and Engineering*, 44, 7875–7893(2019).

45. U. Farooq, T. Hayat, A. Alsaedi and S. Liao, Heat and mass transfer of two-layer flows of third-grade nano-fluids in a vertical channel, *Applied Math. Comp.*, 242, 528-540 (2014).

46. S. Nadeem and S. Saleem, Analytical study of third grade fluid over a rotating vertical cone in the presence of nanoparticles, *Int. J. Heat Mass Transfer*, 85 1041-1048 (2015).

47. W. A. Khan, J. R. Culham and O. D. Makinde, Combined heat and mass transfer of third-grade nanofluids over a convectively-heated stretching permeable surface, *The Canadian Journal of Chemical Engineering*, 93 1880-1888 (2015).

48. S. Qayyum, T. Hayat and A. Alsaedi, Thermal radiation and heat generation/absorption aspects in third grade magneto-nanofluid over a slendering stretching sheet with Newtonian conditions, *Physica B: Condensed Matter*, 537, 139–149 (2018).

49. T. Hayat, S. Ahmad, M. Ijaz Khan and A. Alsaedi, Modeling and analyzing flow of third grade nanofluid due to rotating stretchable disk with chemical reaction and heat source, *Physica B: Condensed Matter*, 537, 116–126 (2018).

50. G. Soave, 20 years of Redlich-Kwong equation of state,*Fluid Phase Equilibria*, 82 345-359 (1993).

51. E. A. Muller and L. A. Estevez, Mixing expansivities and Grashof number in supercritical fluids using cubic equations of state, *Journal of Supercritical Fluids*, 3, 136–142 (1990).

52. S. J. Blundell and K. M. Blundell, Concepts in Thermal Physics, Oxford University Press, UK (2006).

53. V. Rajesh, A.J. Chamkha, Ch. Sridevi, A.F. Al-Mudhaf, A numerical investigation of transient MHD free convective flow of a nanofluid over a moving semi-infinite vertical cylinder, *Engineering Computations*, 34 (5), 1393-1412, (2017).

54. Arshad Khan, Dolat Khan, Ilyas Khan, Farhad Ali, Faizanul Karim and Muhammad Imran, MHD flow of sodium alginate based casson type nanofuid passing through a porous medium with Newtonian heating, *Scientific Reports* 8, 8645, (2018).

55. R.L. Fosdick and K.R. Rajagopal, Thermodynamics and stability of fluids of third grade, *Proc. Royal Society of London. Series A*, 369, 351 – 377 (1980).

56. R. K. Tiwari and M. K. Das, Heat transfer augmentation in a two-sided lid-driven differentially heated square cavity utilizing nanofluids,*Int J Heat Mass Tran*., 50(9–10), 2002–2018 (2007).

57. H. Schlichting and K. Gersten, *Boundary Layer Theory*. New York: Springer-Verlag, (2001).

58. B. Mahanthesh, B. J. Gireesha, Rama Subba Reddy Gorla, Heat and Mass transfer effect on the mixed convective flow of chemically reacting nanofluid past a moving/stationary vertical plate, *Alexandria Engineering Journal*, 55, 569-581 (2016).

59. R. L. Hamilton and O. K. Crosser, Thermal conductivity of heterogeneous two component system. *IndEngChem Fund*, 1, 187–191 (1962).

60. M. Q. Brewster, *Thermal Radiative Transfer and Properties*, John Wiley Son, New York, (1992).

61. B. Carnahan, H. A. Luther and J. O.Wilkes,*Applied Numerical Methods*. New York: John Wiley & Sons, (1969).

62. D. U. Von Rosenberg, *Methods for the Numerical Solution of Partial Differential Equations*, American Elsevier Publishing Company, New York (1969).

63. H. P. Rani and C. N. Kim, Transient convection on a vertical cylinder with variable

viscosity and thermal conductivity, *AIAA J. Thermophysics Heat Transfer*, 22, 254-261 (2008).

64. *NIST (National Institute of Standards and Technology) Chemistry Web Book*, U.S. Secretary of Commerce on behalf of the United States of America, USA (2017).

65. B. E. Poling, J. M. Prausnitz, J. P. O'Connell, *The Properties of Gases and Liquids*, fifth edition, McGraw-Hill, New York, USA, 2001.

66. A. J. Ede,*Advances in Free Convection*, National Engineering Laboratory, East Kilbride, Scotland, UK, 1967.

67. Tamara Bruna, Francisca Maldonado-Bravo, Paul Jara, Nelson Caro, *Silver Nanoparticles and Their Antibacterial Applications,* Int J Mol Sci., 22(13): 7202, 2021.

68. Xi-Feng Zhang, Zhi-Guo Liu, Wei Shen, SangiliyandiGurunathan, Silver *Nanoparticles: Synthesis, Characterization, Properties, Applications, and Therapeutic Approaches,* Int J Mol Sci., 17(9): 1534, 2016.

69. Rajesh, V., Beg, O. A. and Mallesh, M., “Transient nanofluid flow and heat transfer from a moving vertical cylinder in the presence of thermal radiation: Numerical study. *Proceedings of the Institution of Mechanical Engineers, Part N: Journal of Nanomaterials, Nanoengineering and Nanosystems*. 230 (1), pp. 3-16, 2016.

70. G. Janardhana Reddy, BhaskerreddyKethireddy, J.C. Umavathi, Mikhail A. Sheremet, Heat flow visualization for unsteady Casson fluid past a vertical slender hollow cylinder, Thermal Science and Engineering Progress, 5, pp. 172-181, 2018.

71. G. Janardhana Reddy, Mahesh Kumar, J. C. Umavathi and Mikhail Sheremet, Transient Entropy Analysis for the Flow of a Second Grade Fluid Over a Vertical Cylinder, Canadian Journal of Physics 96(9),2018.

72. HussainBasha, G. Janardhana Reddy, N.S. Venkata Narayanan and Mikhail A. Sheremet, Analysis of supercritical free convection in Newtonian and couple stress fluids through EOS approach, International Journal of Heat and Mass Transfer, 152, pp. 119542, 2020.

73. M. Zubair, M. Waqas, T. Hayat, A. Alsaedi and M. Ayub, Stagnation point flow of third grade liquid due to variable thickness a useful application to non-Fourier heat flux approach, Journal of Results in Physics 8, pp. 1010-1016, 2018.

74. T. Hayat, M. Zubair, M. Waqas, A. Alsaedi and M. Ayub, Application of non-Fourier heat flux theory in thermally stratified flow of second grade liquid with variable properties. Chinese journal of Physics 55, pp. 230-241, 2017.

75. T. Hayat, M. Zubair, M. Waqas, A. Alsaedi and M. Ayub, Impact of variable thermal conductivity in doubly stratified chemically reactive flow of second grade fluid subject to non-Fourier heat flux theory. Journal of Molecular Liquids 234, pp. 444-451, 2017.

76. Irfan, M., Farooq, M. A., Mushtaq, A., and Shamsi, Z. H.,Unsteady MHD Bionanofluid Flow in a Porous Medium with Thermal Radiation near a Stretching/Shrinking Sheet. Mathematical Problems in Engineering, 2020, 1–14, 2020.

77. Yadav, D., Chu, Y.-M., and Li, Z.,Examination of the nanofluid convective instability of vertical constant throughflow in a porous medium layer with variable gravity. Applied Nanoscience, 2021.

78. Yadav, D., Numerical solution of the onset of Buoyancy-driven nanofluid convective motion in an anisotropic porous medium layer with variable gravity and internal heating, Heat Transfer, 49 (3), 1170-1191, 2020.

79. Yadav, D., The effect of pulsating throughflow on the onset of magneto convection in a layer of nanofluid confined within a Hele-Shaw cell, Journal of Process Mechanical Engineering 233 (5), 1074–1085, 2019.

80. Zuo, H., Salahshoor, Z., Yadav, D., Hajizadeh, M. R., and Vuong, B. X., Investigation of thermal treatment of hybrid nanoparticles in a domain with different permeabilities. Journal of Thermal Analysis and Calorimetry, 2020.

81. Yadav, D., Influence of anisotropy on the Jeffrey fluid convection in a horizontal rotary porous layer. Heat Transfer, 50(5), 4595–4606, 2021.

82. Yadav, D., Wang, J., Bhargava, R., Lee, J. and Cho, H. H., “Numerical investigation of the effect of magnetic field on the onset of nanofluid convection”, Applied Thermal Engineering, 103, 1441-1449, 2016.